Journal of
Materials Chemistry A

ROYAL SOCIETY
OF CHEMISTRY

PAPER

View Article Online
View Journal

Check for updates

Cite this: DOI: 10.1039/d5ta08701e

Engineering of Li$^+$-selective quasi-solid electrolytes *via* zwitterion and poly(ethylene glycol) co-grafting on poly(arylene ether sulfone) for high-performance lithium–sulfur batteries

Anh Le Mong,[a] Jong Chan Shin,[b] Minjae Lee[b] and Dukjoon Kim*[a]

Received 27th October 2025
Accepted 19th January 2026

DOI: 10.1039/d5ta08701e

rsc.li/materials-a

The creation of a highly efficient lithium-ion-conductive solid and/or quasi-solid electrolyte with effective polysulfide (PS) suppression is essential for stable lithium–sulfur (Li–S) batteries. This study presents a self-assembled quasi-solid electrolyte formed by co-grafting zwitterion (ZW) and poly(ethylene glycol) (PEG) segments onto a durable poly(arylene ether sulfone) (PAES) backbone, denoted as PAES-*co*-(ZW/PEG)$_2$. Within the robust PAES framework, Li-ion conductive (ZW/PEG) domains are generated through phase separation assisted by an ionic liquid and ethylene carbonate, ensuring both excellent ionic conductivity and mechanical integrity. The ZW segments effectively restrict PS migration and promote selective Li-ion transport *via* electrostatic interactions between delocalized anionic sites and Li-ions. The PAES-*co*-(ZW/PEG)$_2$ membrane exhibits a high Li$^+$ transference number (0.752), superior ionic conductivity (1.58 mS cm^{-1}), and favorable mechanical strength (Young's modulus: 15 MPa; tensile strength: 1.8 MPa). Furthermore, it provides remarkable PS-blocking performance ($\sim$3.418 × 10^{-5} cm^2 s^{-1}) and excellent oxidative stability (5.28 V). Li–S cells employing this electrolyte demonstrate stable cycling over 350 cycles with 93% capacity retention and outstanding rate capability up to 5 C, indicating strong potential for advanced Li–S battery systems.

Introduction

The transition toward transportation electrification and the decarbonization of electricity generation is accelerating the search for next-generation battery systems surpassing current lithium-ion technologies.[1,2] Among these, lithium–sulfur batteries (LSBs), which consist of a lithium metal anode, sulfur cathode, and separator fully dipped in organic liquid electrolyte, show significant promise for future energy storage solutions, especially for grid-scale or large-scale implementations.[3] The lithium anode offers a maximum capacity of 3860 mAh g^{-1}, significantly exceeding 372 mAh g^{-1} of the graphite-based electrode, together with an extremely low electrochemical standard potential of −3.04 V with respect to the standard hydrogen electrode.[4,5] Meanwhile, sulfur and/or sulfur-based compounds as a positive electrode are abundant, inexpensive, and lighter than the metal oxides used in Li-ion batteries.[4,6] Consequently, LSBs can achieve 2600 Wh kg^{-1} (maximum energy density), markedly exceeding 250–300 Wh kg^{-1} of conventional lithium-ion batteries, and provide additional benefits in terms of light weight and cost-effectiveness.[7] However, LSBs are still in the research and development phase and also face several challenges that hinder their widespread adoption and commercialization.[8] Firstly, the use of organic liquid electrolytes not only poses a fire risk and explosions due to their flammability but also leads to the dissolution of intermediate sulfur compounds (polysulfides, PS).[9–12] These polysulfides can migrate between the anode and cathode during charge and discharge cycles, resulting in the loss of active material and a decline in battery capacity over time. Secondly, lithium anodes are prone to forming dendrites–needle-like structures that grow during charging due to low lithium ion conduction and side reactions between the anode surface and organic liquid electrolyte.[13–18] Such dendrites are capable of penetrating the separator, resulting in short circuits, which can lead to battery failure or even safety hazards. Finally, the sulfur cathode exhibits low conductivity and undergoes significant volume expansion ($\sim$80%) when reacting with lithium to form Li$_2$S. This expansion induces mechanical stress and structural changes within the cathode, which can result in cracking and the loss of electrical contact.[19,20] These effects contribute to a reduction in the LSB's capacity and lifespan.

Targeting this issue, replacing organic liquid electrolytes with solid and/or quasi-solid polymeric electrolytes (SPEs) in LSBs presents several advantages that address key challenges

---

[a] School of Chemical Engineering, Sungkyunkwan University, Suwon, Gyeonggi, 16419, Republic of Korea. E-mail: djkim@skku.edu

[b] Department of Energy Science & Engineering, Department of Chemistry, Kunsan National University, Gunsan, Jeollabuk-do, 54150, Republic of Korea. E-mail: minjae@kunsan.ac.kr

associated with LSB technology.[21,22] However, the design of SPEs that simultaneously exhibit (i) a mechanically robust modulus to suppress dendrite growth; (ii) strong chemical and/or electrochemical stability at the Li-anode interface; and (iii) adequate ionic conductivity for reliable cell performance remains challenging, owing to the inherent trade-offs among these material properties.[23] Consequently, alternative solid electrolytes exhibiting high ionic conductivity, coupled with superior electrochemical, mechanical, thermal, and chemical robustness, must be developed to enable the large-scale deployment of LSBs. A wide range of strategies has been proposed and studied to simultaneously improve not only ionic conductivity but also mechanical robustness of SPEs. These strategies include (i) integration of nanofillers for enhanced mechanical stability, (ii) designing novel hybrid materials, (iii) incorporating ionic liquid plasticizers to boost ion conductivity, and/or (iv) a hybrid strategy combining these techniques.[24–26] Unfortunately, these methods often introduce additional and complex fabrication procedures to achieve uniform additive dispersion throughout the membrane. While these methods may yield promising results at a small scale, where solvent casting and ultrasonic mixing are used to prevent particle agglomeration, scaling up to commercial quantities presents significant challenges, as these processes are often impractical or costly on a larger scale.[27,28]

On the other hand, as there are opposite migrations of Li-ions and counter anions toward two electrodes during charge and discharge cycling processes, lithium ions contribute less to the total ionic conductivity than counter anions (only about 20% of the overall conduction is provided by Li-cations), thus leading to a low fraction of the total charge being transported by Li-ions (lithium ion transference number, $t_{\mathrm{Li}^+} = 0.1\text{–}0.2$).[29] A low lithium transference number limits the battery's efficiency in transporting lithium ions, leading to reduced power, lower efficiency, and potential long-term instability.[30] Improving t_{Li^+} is crucial for enhancing the performance of solid-state LSBs. Researchers focus on developing new materials that restrict the movement of non-lithium ions, optimizing the structure of solid electrolytes, and enhancing lithium-ion selectivity through surface treatments, doping, and composite designs. These approaches are intended to improve the efficiency and electrochemical cell performance of Li-based batteries in the solid-state. However, each of the strategies to improve the lithium transference number comes with trade-offs. These include lower overall conductivity, interfacial issues, mechanical instability, cost, and fabrication complexity. Optimizing these techniques requires balancing the improved lithium-ion transport with the practical challenges they introduce.[31,32]

According to this trend, an innovative method for improving effective Li-ion conductivity (superior σ and high t_{Li^+}) and mechanical properties of SPEs without incorporating nanofillers involves employing a self-assembled copolymer structure.[33–36] Copolymer electrolytes typically consist of two or more chemically different polymers, forming a block and/or graft copolymer. These copolymers can self-assemble into nanostructures, creating ordered microphase-separated domains that define selective channels. One component of the copolymer contains ion-conducting materials that can be engineered to create pathways that preferentially allow lithium-ion movement and restrict anion transport. The other is non-conducting and provides mechanical strength and structural integrity and enhances thermal and electrochemical stability of solid electrolyte. In this approach, a mechanically robust segment is covalently integrated with ion-conducting segments.[37–39] The intrinsic microphase separation within these materials facilitates the independent optimization of both mechanical and ionic conductivity properties of SPE. Following this method, both conductive poly(ethylene glycol) (PEG) and ((3-(pyrrolidin-1-ium-1-yl)propyl)sulfonyl) ((trifluoromethyl) sulfonyl) amide zwitterionic (ZW) segments were anchored onto a mechanically robust poly(arylene ether sulfone) (PAES) main–chain, forming (PAES-*co*-(ZW/PEG)$_2$), with the incorporation of a threshold ethylene carbonate (EC) content and PYR–Tf$_2$N, a *N*-butyl-*N*-methylpyrrolidinium bis(trifluoromethanesulfonyl) imide-based ionic liquid (IL) to achieve a robust quasi-solid electrolyte with high single Li-ion conduction. PAES-*co*-(ZW/PEG)$_2$ can self-assemble into nanostructures, creating microphase-separated regions (mechanically reinforced PAES and selective Li-ion conductive PEG/ZW regions) due to heterogeneous chemical compatibilities between the PAES backbone and PEG and ZW graft chains with the IL–EC blend (see Fig. 1). The PAES regions form a supportive matrix that isolates the conducting channels for mechanical reinforcement and enhances thermal and electrochemical stability of the electrolyte membrane. In ion-conducting regions, the Li-ion transport in PEG domains is controlled through the segmental α-relaxations of amorphous PEG chains, mediated by coordination between Li-ions and –O– ligands of the ethylene glycol repeat units. These electron-rich oxygen atoms interact with Li-ions, forming coordination complexes that guide the lithium through the membrane.[40] The flexibility of PEG chains facilitates the mobility of coordinated lithium ions, allowing them to migrate between coordination sites. In addition, the ZW graft-chains positively contribute to facilitating selective Li-ion transport. The t_{Li^+} of PAES-*co*-(ZW/PEG)$_2$ membrane is also increased by limiting the mobility of Tf$_2$N anions *via* electrostatic interaction from the cation site and promoting selective Li-ion transport from delocalization of the negative charge across four oxygen atoms and one nitrogen atom within the anionic site of ZWs.[41] This delocalization not only reduces the local electrostatic attraction between the anions and Li-ions but also establishes a more stable coordination environment for Li-ions. As a result, Li-ions more easily move from one coordination site to another without being hindered by the strong attraction of a localized anion.[42,43] This promotes the selective transport of lithium ions, improving the transference number.

Furthermore, the presence of ZW graft-chains concurrently fulfills efficient polysulfide blockage. Polysulfide anions function as electron donors anchored to the pyrrolidinium rings, whereas Li-ions preferentially coordinate with the Tf$_2$N anion site of ZW, thereby contributing to the promotion of lithium polysulfide dissociation, the facilitation of Li-ion mobility, and the suppression of polysulfide migration. Besides,

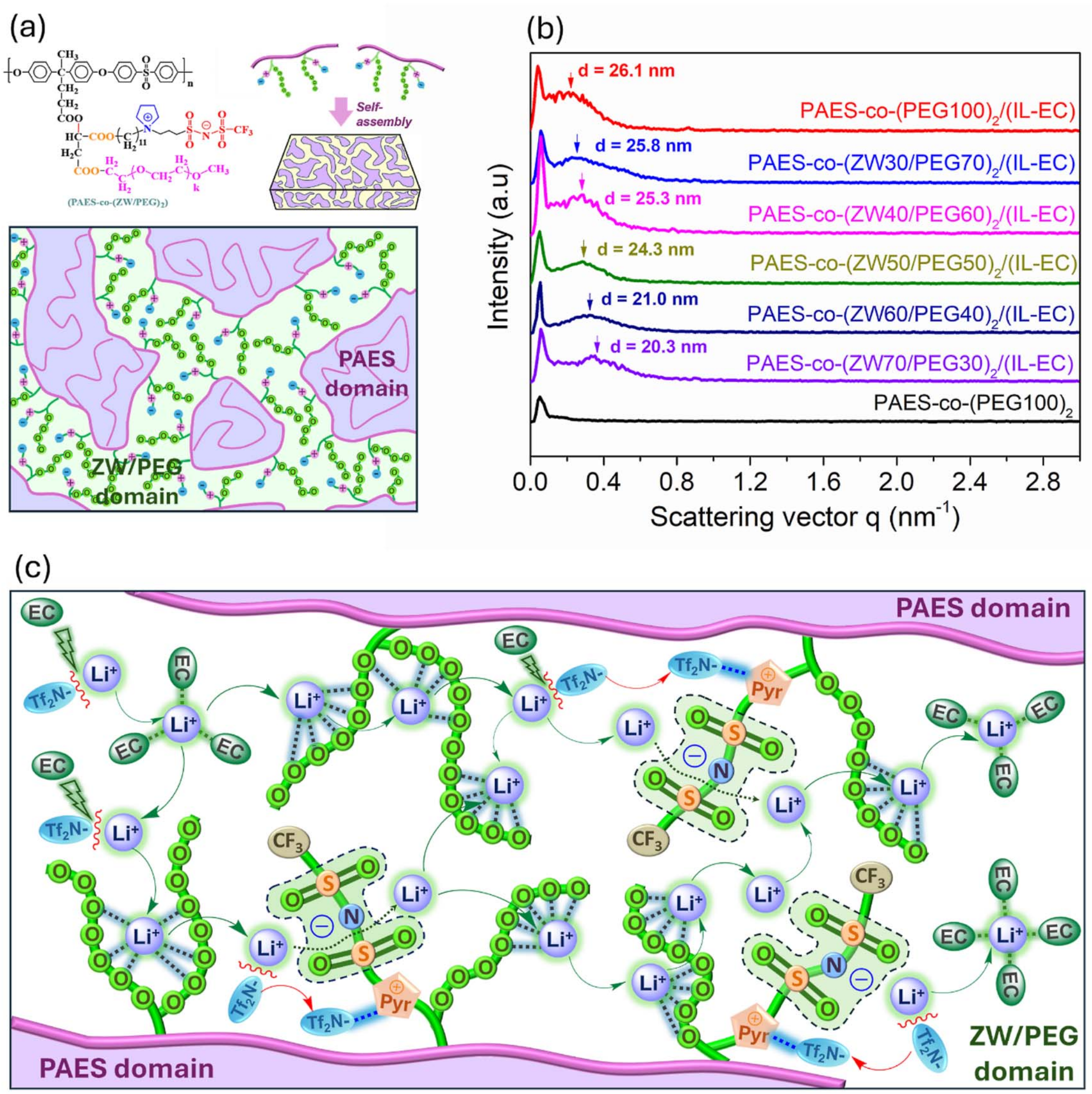

Fig. 1 (a) Illustration of PAES and PEG domain formation *via* self-assembly of PAES-*co*-(ZW/PEG)$_2$ membranes; (b) phase separation behavior of PAES-*co*-(ZW/PEG)$_2$ membranes with various ZW/PEG ratios at 70 wt% IL–EC using SAXS analysis; and (c) illustration of the Li-ion transporting mechanism of the PAES-*co*-(ZW/PEG)$_2$ membrane in the presence of IL–EC.

incorporation of an appropriate amount of IL–EC contributes to facilitating microphase separation and concurrently accelerating Li-ion migration and improving thermal robustness and the electrochemical stability window because of the plasticizing effect of IL and shielding effect of EC.[44] By the high dielectric influence of EC, Li-salt dissociation is enhanced while the formation of aggregated [Li-ion/$(Tf_2N^-)_x$, $x \leq 3$] complexes is effectively suppressed, resulting in abundant free Li-ions that interact efficiently with PEG segments supported by [Li-ion/$(EC)_x$, $x < 5$] complexes through a shielding mechanism and high motion of PEG segments *via* the plasticizing effect of IL.[45–47] For improved LSB performance, PAES-*co*-(ZW/PEG)$_2$ was investigated as a cathodic binder. This strategy enhances cathode-SPE interfacial compatibility and promotes Li-ion conduction in cathode areas rich in the insulating active material (S), when PAES-*co*-(ZW/PEG)$_2$ is used in both the binder and SPE. Attributed to these favorable features, the notable advantages of as-synthesized flexible PAES-*co*-(ZW/PEG)$_2$ in enhanced effective Li-ion conduction and effective polysulfide management offer a promising route toward robust solution-based sulfur chemistry and high-efficiency LSBs. In particular, PAES-*co*-(ZW/PEG)$_2$ is synthesized *via* conventional polymer chemistry and fabricated through a solution-casting process compatible with industrial production. Importantly, despite incorporating a high content of IL–EC, the resulting membrane retains a solid-state form with good mechanical integrity and flexibility, enabling the fabrication of large-area, free-standing films and compatibility with roll-to-roll processing. These features distinguish PAES-*co*-(ZW/PEG)$_2$ from many previously reported solid electrolytes and highlight its strong potential for scalable and practical LSB applications.

Results and discussion

Structural characterization of molecules

The stepwise synthesis procedure of PAES-*co*-$(ZW/PEG)_2$ is schematically provided in Fig. S1. First of all, the zwitterion precursor *N*-(((3-[1-(11-hydroxyundecyl) pyrrolidinium)] propyl) sulfonyl) trifluoromethane-sulfonyl) imide (ZW) was successfully synthesized *via* a quaternization reaction between 1-(11′-hydroxyundecyl) pyrrolidine and potassium (3-chloropropylsulfonyl) (trifluoromethyl-sulfonyl) imide in acetonitrile under reflux conditions for 4 days (see Fig. S1). After dissolution in acetonitrile, the crude compound underwent purification by reprecipitation, using diethyl ether and deionized water, yielding a solid in good purity. The synthesized ZW was characterized using ^{1}H-NMR spectroscopy, as shown in Fig. S2.

The successful co-grafting reaction between carboxylic acid functionalized PAES and the zwitterion precursor/PEG gave the final product PAES-*co*-$(ZW/PEG)_2$. The chemical structure was confirmed by the characteristic NMR and FT-IR spectra as indicated in Fig. S3. First, the PAES backbone was identified by the signals appearing at 7.19, 7.91, and 6.96 ppm, representing aromatic protons in the ortho, meta, and para locations, respectively (see Fig. S3a). Also, both ZW and PEG segments were recognized by the appearance of some proton peaks of methylene ($-CH_2-$) groups in PEG (3.43 and 3.52 ppm) and methylene ($-CH_2-$) (3.22 and 3.04 ppm) and methyl ($-CH_3$) groups (1.61 and 1.03 ppm) in PYR, respectively. In addition, the co-grafting ZW/PEG ratio was systematically controlled at molar ratios of 70 : 30, 60 : 40, 50 : 50, 40 : 60, 30 : 70, and 0 : 100, ensuring that the total number of moles equaled the mole number of dual carboxylic acid pendant groups in PAES. The nomenclature for all prepared electrolyte membranes followed the format PAES-*co*-$(ZWxx/PEGyy)_2$, where *xx*:*yy* denotes the molar ratios of the co-grafted ZW to PEG. The ratio of grafted ZW to PEG in PAES-*co*-$(ZW/PEG)_2$ was additionally verified through NMR analysis (refer to Fig. S4 and Table S1). FT-IR also gave a clue of successful esterification reaction formations which surely confirm the segment linkage formation recognized by stretching vibration (C–O in the ester group) at 1670 cm^{-1}. The PEG graft chains were confirmed by the C–O–C stretching signal appearing at 1480 cm^{-1}. The ZW segments were recognized by some recorded peaks at 1350 cm^{-1} (stretching C–N in the PYR^+ cationic site), 1110 cm^{-1} (stretching N–S in the $Tf2N^-$ anion), and 980 cm^{-1} (stretching C–F in the Tf_2N^- anionic site) (see Fig. S3b). ^{13}C-NMR spectroscopy was also performed to verify the esterification reaction in PAES-*co*-(ZW/PEG)2, and the results are presented in Fig. S5. A clear resonance at 173.1 ppm is observed, which is well assigned to the ester carbonyl (–COO–) carbon according to established literature values for ester-containing polymers. The appearance of this characteristic ester signal, together with the disappearance of carboxylic acid proton signals in the corresponding ^{1}H-NMR spectrum and the complementary FTIR results, provides strong evidence for the successful esterification of ZW/PEG side chains onto the PAES backbone.

Self-assembly ability

Self-assembled electrolyte membranes play an important role in Li-ion conductive domain formation to facilitate Li-ion transport. From Fig. 1a, the PAES-*co*-$(ZW/PEG)_2$ membranes incorporating IL–EC are expected to create Li-ion transport-active ZW/PEG regions separated from robust PAES domains as a result of the pronounced differences in chemical and physical compatibility between ZW/PEG segments and the PAES backbone with IL–EC. In the PAES-*co*-$(ZW/PEG)_2$ membrane, 70 wt% IL–EC incorporation favored the formation of ZW/PEG domains, as evidenced by the discernible peak in the SAXS curves (see Fig. 1b). In contrast, the SAXS curve of the PAES-*co*-$(ZW/PEG)_2$ membrane without adding IL–EC did not exhibit such a peak. Conversely, the spacing of ZW/PEG regions in the PAES-*co*-$(ZW/PEG)_2$ membrane exhibited a slight dependence on the co-grafting ZW/PEG ratio. The dimensional spacing of ZW/PEG domains was increased from 20.3 nm to 26.1 nm with the increasing amount of PEG segments. Notably, the PAES-*co*-$(ZW/PEG)_2$ membrane at ZW/PEG ratios of 30 : 70 and 40 : 60 demonstrated a significant enlargement in ZW/PEG domain size, measuring 25.8 and 25.3 nm, respectively. These dimensions closely approached the ZW/PEG domain size of the PAES-*co*-$(PEG)_2$ membrane (26.1 nm), potentially contributing to enhanced Li transport (see Fig. 1c).

Investigation of lithium-ion transport

Ionic conductivity. As only lithium cation movement is necessary to enable effective charge/discharge cycles, single lithium-ion conduction in solid electrolytes is essential in influencing the performance of LSBs. Solid electrolyte membranes exhibiting high lithium-ion conduction are favored for facilitating faster charging and discharging processes to enhance the efficiency and overall performance of battery cells. In general, lithium-ion conduction is typically assessed through measurements of ionic conductivity (σ), lithium transference number (t_{Li^+}), and interfacial resistance (R_i). To start with, the σ of PAES-*co*-$(ZW/PEG)_2$ membrane at various ZW/PEG ratios was determined using Nyquist plots (refer to Fig. 2a) collected from the impedance test and these results are shown in Fig. 2b. In this study, the mixture of ionic IL and EC at 7 : 3 (v/v) was chosen to enhance σ and t_{Li^+} because the addition of EC, characterized by its high dielectric constant ($\varepsilon = 89$), significantly contributes to enhancement of $LiTf_2N$ dissociation to produce a great number of Li-ions in single-ion form. The IL–EC mixture was introduced into the PAES-*co*-$(ZW/PEG)_2$ membrane at 70 wt% not only to promote conductive domain formation at the solid physical state but also to improve segmental motion of PEG. As displayed in Fig. 2b, the σ of the PAES-*co*-$(ZW/PEG)_2$ membrane was induced until a co-grafting ZW/PEG ratio of 40 : 60 and then reduced with the increasing ZW/PEG ratio. The observed enhancement in ionic conductivity is due to the formation of large ZW/PEG domains, which facilitate the formation of facile pathways for lithium transport (see Fig. 1c). Furthermore, the synergistic effect between ZW and PEG on Li-ion migration was heightened, whereby Li-ion transport is facilitated not only by ionic interactions of Li-ions with the Tf_2N^- anion of ZW (Li^+/

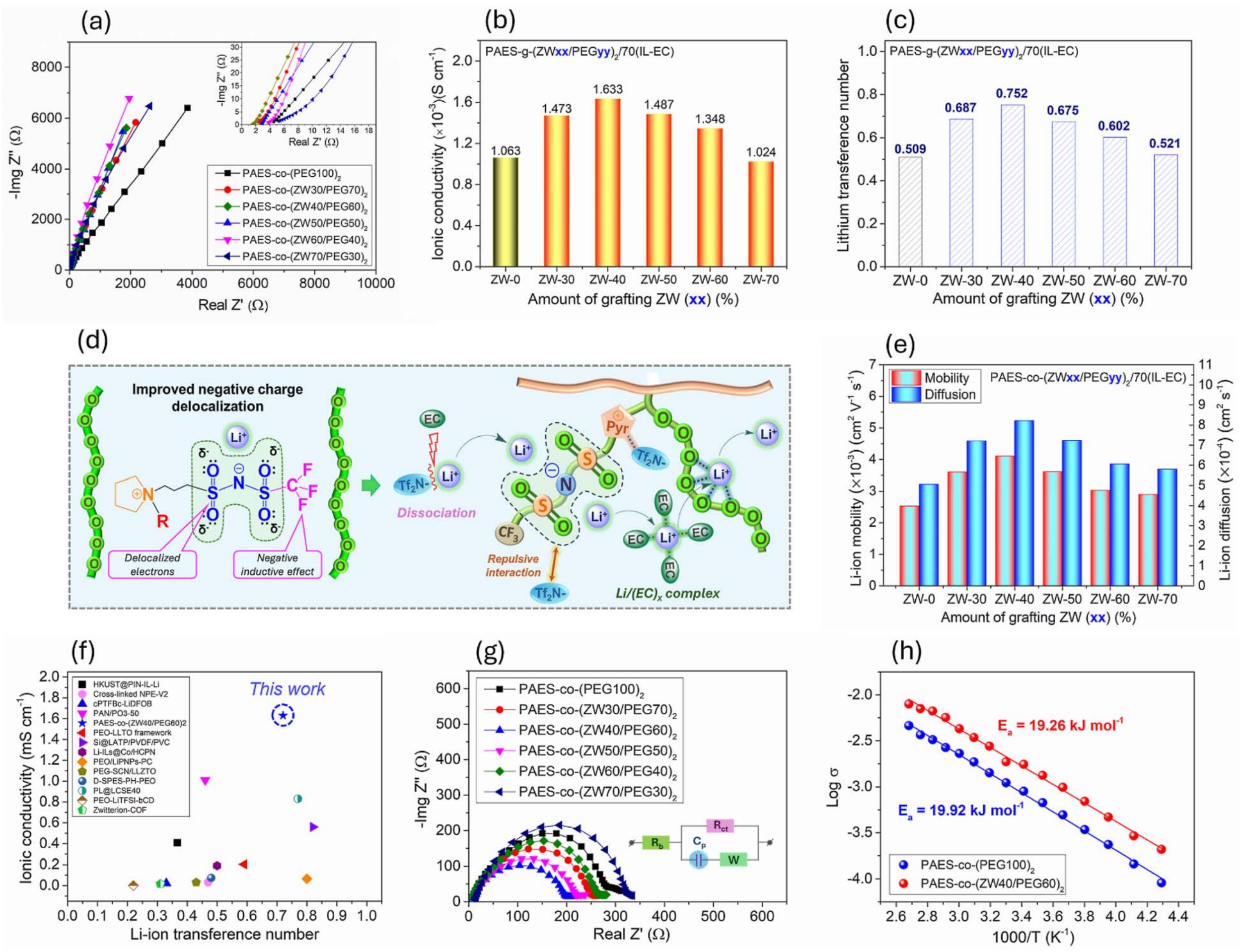

Fig. 2 (a) Nyquist plot; (b) ionic conductivity; (c) Li-ion transference number; (d) illustration of the Li-ion transporting mechanism under delocalization and ethyl carbonate effects; (e) Li-ion mobility and diffusion; (f) comparison of ionic conductivity (σ) and the Li-ion transference number of the PAES-*co*-(ZW/PEG)$_2$ membrane with those of other electrolytes recently reported; (g) interfacial resistance of PAES-co-(ZW/PEG)$_2$ membranes containing various IL–EC contents; and (h) ionic conductivity and temperature relationship.

Tf_2N^-(ZW)) but also by ion–polar interactions of Li$^+$-cations with ether functionalities (Li$^+$/O(PEG)) *via* the dynamic motion of PEG chains. Conversely, at ZW/PEG ratios exceeding 40 : 60, a decreasing trend in ionic conductivity was observed due to the reduced spacing of ZW/PEG domains and higher ion–ion interactions (Li$^+$/Tf_2N^-(ZW)) compared to ion–dipole interactions (Li$^+$/O(PEG)), resulting in slower Li-ion transport. Among all prepared membranes, the PAES-*co*-(ZW/PEG)$_2$ membranes at a ZW/PEG ratio of 40 : 60 (PAES-*co*-(ZW40/PEG60)$_2$) had the most outstanding conductivity of 1.583 S cm^{-1} at room temperature, comparable to the pure electrolyte, reflecting both superior compatibility and effective Li-ion transport.

Lithium transference number. Acceleration of single Li-ion transport (t_{Li^+}) is required to ensure proper performance of electrolyte membranes in lithium based secondary batteries. Low t_{Li^+} could cause the generation of anion concentration gradients, thereby resulting in interfacial polarization and lithium dendrite formation and growth during cycling in LSBs. Therefore, improvement of t_{Li^+} is desirable for stabilizing the electrolyte/Li electrode interface and limiting lithium dendrite propagation. The t_{Li^+} of the PAES-*co*-(ZW/PEG)$_2$ membrane at various co-grafting ZW/PEG ratios was calculated from the measured values of the parameters used in eqn (7) through chronoamperometry (CA) and impedance tests (refer to Fig. S6) and these corresponding results are presented in Fig. 2c. Generally, all prepared PAES-*co*-(ZW/PEG)$_2$ membranes exhibited significantly higher t_{Li^+} values compared to the PAES-*co*-(PEG)$_2$ membrane, primarily due to the influence of ZW graft-chains. These chains not only immobilize the migration of Tf_2N^- anions through strong ionic interactions between the PYR cationic site of ZW and Tf_2N^- anions but also facilitate Li-ion transport to coordinate with oxygen atoms of PEG segments *via* ionic interactions of Li-ions with the anionic sites of ZW. The presence of the delocalized negative charge on the anionic site (one nitrogen and four oxygen atoms) of ZW groups promotes its interactions with Li-ions and immobilizes Tf_2N-anion movements due to its substantial anionic size. Additionally, the anionic site of ZW groups enhances the dissociation of ionic aggregations [Li$^+$–O/(Tf_2N^-)$_{1\div3}$], thereby generating a significant number of free Li-ions for facile transport within PEG domains, consequently leading to improved transference number values (refer to Fig. 2d).

Furthermore, the t_{Li^+} of all prepared PAES-*co*-(ZW/PEG)$_2$ membranes first rose and subsequently declined as the ZW/PEG ratio increased. Notably, PAES-*co*-(ZW/PEG)$_2$ membranes at a ZW/PEG ratio of 40 : 60 exhibited the highest t_{Li^+} value of 0.752, surpassing that of the PAES-*co*-(PEG100)$_2$ membrane (0.501), owing to the synergistic effect between ZW and the segmental motion of PEG (see Fig. 2c). This finding suggests that Tf_2N^- anion diffusion is constrained within the PAES-*co*-(ZW/PEG)$_2$ membrane, while Li-ion transport is facilitated through the co-grafting of ZW and PEG. To provide more evidence, the substantiation of the potential mechanism was achieved by assessing lithium diffusion coefficients using transient ion current (TIC) (refer to Fig. S7). Li-ion diffusion coefficients (D_{Li^+}) and Li-ion mobility (μ_{Li^+}) of both PAES-*co*-(PEG100)$_2$ and PAES-*co*-(ZW40/PEG60)$_2$ membranes were evaluated and are displayed in Fig. 2e. The PAES-*co*-(ZW40/PEG60)$_2$ membrane exhibited higher lithium mobility (4.11×10^{-3} cm^2 V^{-1} s^{-1}) and diffusion coefficient (8.22×10^{-4} cm^2 V^{-1} s^{-1}), facilitating enhanced Li-ion transport (resulting in higher σ and t_{Li^+}).

In comparison, although the t_{Li^+} of the PAES-*co*-(ZW40/PEG60)$_2$ membrane is not unique, this value, along with high σ, has still been significantly higher than that of other solid electrolytes, which was rarely achieved in previously published literature (refer to Fig. 2f).[48–57] The superior Li-ion conduction can be ascribed to several influencing factors: (i) the augmented segmental flexibility of PEG segments attributable to the superior plasticizing influence of IL–EC; (ii) increased dissociation of salt and ionic aggregation to enhance interactions between Li^+/anionic sites of ZW *via* delocalized charge distribution; and (iii) limitation of Tf_2N^- mobility by increasing the size of anionic sites in ZW groups (see Fig. 1 and 2d).

Interfacial resistance. Interfacial resistance, referring to the resistance encountered at the interfaces between solid electrolyte and electrodes, is crucial to evaluate the performance and lifespan of LSBs. As the Li-anode has high activity, unwanted reactions often occur to produce a poorly stable solid electrolyte interphase at the Li-electrode/electrolyte membrane interface during charge/discharge cycling. High interfacial resistance at the Li-anode/electrolyte interface can lead to decreased LSB performance, reduced efficiency, and increased heat generation during operation. Therefore, the interfacial resistance of the prepared PAES-*co*-(ZW/PEG)$_2$ membranes was comparatively investigated at various ZW/PEG ratios by an impedance test. A simplified equivalent circuit was employed to fit the collected EIS data (Fig. 2g, inset), where R_b, R_i, C_p, and Z_w denote the respective bulk resistance, interface resistance, the capacitance of the electric double layer and Warburg diffusion resistance, respectively. As depicted in Fig. 2g, the interfacial resistance of PAES-*co*-(ZW/PEG)$_2$ membranes initially decreased and subsequently increased upon further increasing the ZW/PEG ratio. Among them, the PAES-*co*-(ZW/PEG)$_2$ membrane at a 40 : 60 ZW/PEG ratio has the lowest interfacial resistance (196 Ω), lower than that of the PAES-*co*-(PEG100)$_2$ membrane (273 Ω) at a composition of 70 wt% IL–EC. The lowest interfacial resistance of the PAES-*co*-(ZW40/PEG60)$_2$ membrane at a 40 : 60 ZW/PEG ratio can be primarily attributed to the co-grafting of PEG segments and ZW groups. This co-grafting facilitates Li-ion transport at the interface by creating Li-ion conductive pathways through phase separation and enhancing the dissociation of salt and ionic aggregations through the delocalization of negative charge distribution from ZW groups.

Lithium transporting mechanism. Fig. 2h presents the ionic conductive ability of PAES-*co*-(PEG100)$_2$ and PAES-*co*-(ZW40/PEG60)$_2$ membranes in a wide range of temperature from −40 to 90 °C. Both membranes exhibit a rise in ionic conductivity with rising temperature. Within the low temperature region (−40 °C), both membranes show relatively low ionic conductivities (0.091×10^{-3} and 0.158×10^{-3} S cm^{-1} for PAES-*co*-(PEG100)$_2$ and PAES-*co*-(ZW40/PEG60)$_2$ membranes, respectively). As the temperature increases to 90 °C, there is a significant rise in ionic conductivity for both membranes (4.628×10^{-3} and 7.947×10^{-3} S cm^{-1} for PAES-*co*-(PEG100)$_2$ and PAES-*co*-(ZW40/PEG60)$_2$ membranes, respectively) (see Fig. S8). This trend is attributed to the facilitated segmental mobility of PEG chains, which promotes migration of ions with increasing temperature. Additionally, the increased degree of salt dissociation produces a greater availability of free lithium ions for ionic transport. The kinetic energy of Li-ions also increases, leading to greater ion movement at higher temperature. The PAES-*co*-(ZW40/PEG60)$_2$ membrane demonstrates higher ionic conductivity than the PAES-*co*-(PEG100)$_2$ membrane across the entire measured temperature range. This improvement is due to the presence of ZW groups, which enhance the dissociation of lithium salt, creating more mobile lithium ions for conduction. Fitting the membranes' ionic conductivity to the Arrhenius model yielded a linear $\log(\sigma)$–$1000/T$ plot, from which activation energies (E_a) of 19.92 and 19.26 kJ mol^{-1} were obtained for PAES-*co*-(PEG100)$_2$ and PAES-*co*-(ZW40/PEG60)$_2$ membranes, respectively. To experimentally support this mechanism, multiple complementary characterization techniques were conducted as shown in Fig. S9. The TEM image confirmed the formation of microphase-separated PEG-rich domains, which serve as continuous Li^+-conductive channels. Raman spectroscopy and XPS provide direct evidence of Li^+ coordination with PEG ether oxygens, ZW moieties, and EC molecules. Importantly, ^{7}Li-NMR spectroscopy reveals a single resonance peak at ∼0.54 ppm, indicating fast Li^+ exchange among different coordination environments, including PEG–Li^+, ZW-associated Li^+, and EC–Li^+ species. Collectively, these results demonstrate that Li^+ transport is governed by migration through interconnected amorphous PEG domains, while EC and ZW groups promote salt dissociation and stabilize mobile Li^+ species, thereby facilitating efficient ion transport.

Mechanical performance and thermal stability

Mechanical characteristics of solid electrolytes in lithium–sulfur batteries play a crucial role in retaining structural integrity, preventing dendrite formation, ensuring interface stability, and improving overall battery safety and performance. Mechanical performance metrics (elongation at failure, Young's modulus, and tensile strength) of PAES-*co*-(PEG100)$_2$ and PAES-*co*-(ZW40/PEG60)$_2$ membranes were investigated using UTM tests, and the results are shown in Fig. 3a. From the UTM curves of the membranes, the PAES-*co*-(PEG100)$_2$ membrane exhibits Young's modulus, elongation at failure, and tensile strength values of 50%, 11.0 MPa, and 1.0 MPa, respectively. In contrast, the PAES-*co*-(ZW40/PEG60)$_2$ membrane shows a higher elongation at failure of 35%, Young's modulus of 15.0 MPa, and tensile strength of 1.8 MPa. These findings suggest that the PAES-*co*-(ZW40/PEG60)$_2$ membrane has significantly improved fracture toughness, attributed to the distortion and stress relaxation of PAES induced by the reduced amount of soft PEG segments. The high tensile strength makes the polymer membrane suitable as a SPE in terms of safety concerns. Compared with other previously published reports, the PAES-*co*-(ZW40/PEG60)$_2$ membrane has sufficiently high mechanical properties, enough to support cell assembly, storage, and long-term cycling operation with robust suppression of Li-dendrite development (see Table S2).

Both PAES-*co*-(PEG100)$_2$ and PAES-*co*-(ZW40/PEG60)$_2$ demonstrated excellent transparency and mechanical flexibility, enabling repeated twisting around a 5.0 mm-diameter rod while preserving their original form (see Fig. 3b). In addition, the tailored membranes exhibited robust mechanical stability, sustaining substantial bending or stretching without compromising their morphology. These observations suggest that the PAES-*co*-(ZW40/PEG60)$_2$ membranes have adequate flexibility for prospective applications in LSBs.

Thermal stability of the solid electrolyte directly governs the safety, performance, longevity, and versatility of LSBs. Solid electrolytes with high thermal stability, including high decomposition temperature, thermal transition behavior, thermal dimensional swelling, and strong flammable resistance, are essential to prevent loss of ionic conductivity and thermal runaway – a condition where the battery heats up

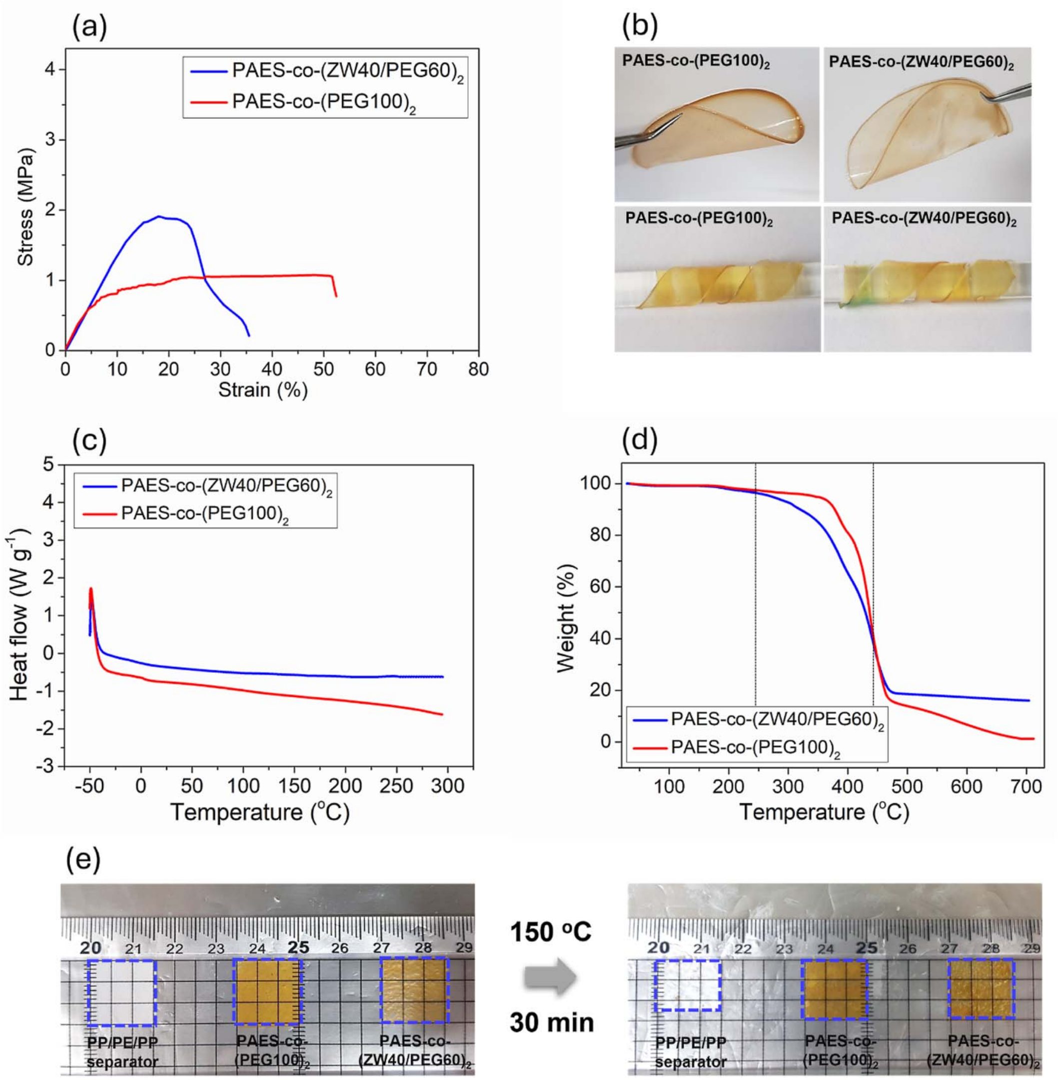

Fig. 3 (a) UTM curves; (b) bending and twisting test; (c) DSC curves; (d) TGA curves; and (e) thermal shrinkage of PAES-*co*-(PEG100)$_2$ and PAES-*co*-(ZW40/PEG60)$_2$ membranes containing 70 wt% IL–EC contents.

uncontrollably, potentially leading to fires or explosions. Accordingly, the decomposition temperature and thermal transition behavior of both PAES-*co*-$(PEG100)_2$ and PAES-*co*-$(ZW40/PEG60)_2$ membranes were investigated by TGA and DSC analysis, and their results are presented in Fig. 3c and d. From DSC curves, the absence of melting and glass transition between −50 and 300 °C suggests that all prepared membranes are entirely amorphous, with no detectable crystalline domains, originating from the plasticizing influence of the IL–EC system. From Fig. 3d, the thermal decomposition of both PAES-*co*-$(PEG100)_2$ and PAES-*co*-$(ZW40/PEG60)_2$ membranes can be divided into two distinct stages according to the temperature range and mass-loss behavior. (i) Although a minor mass loss of approximately 1–3 wt% is observed at lower temperatures, this weight change is attributed to instrumental uncertainty and/or the removal of physically adsorbed species, rather than to the thermal degradation of the PAES-*co*-$(ZW40/PEG60)_2$ backbone. Accordingly, the primary thermal decomposition stage is defined to commence at ∼250 °C, where chemically meaningful degradation processes occur. The major mass loss takes place between ∼250 and 450 °C, accounting for approximately 70–75 wt% of the total weight. This stage corresponds to the thermal decomposition of PEG segments, zwitterionic side chains, and the onset of PAES backbone degradation, consistent with reported degradation temperatures of PEG-based and sulfonyl-containing polymers. (ii) At above 450 °C, a gradual mass loss is observed. The PAES-*co*-$(ZW40/PEG60)_2$ membrane retains approximately 15–18 wt% residues at 700 °C, which is attributed to progressive carbonization and the formation of thermally stable inorganic and carbonaceous residues following complete polymer decomposition.[58–60]

The thermal resistance properties of the prepared quasi-solid electrolytes were assessed by conducting thermal shrinkage tests on the commercial PP separator and PAES-*co*-$(PEG100)_2$ and PAES-*co*-$(ZW40/PEG60)_2$ membranes at 150 °C for 30 min. As displayed in Fig. 3e, an obvious shrinkage occurred in the commercial separator, resulting in 75% dimensional retention, while the PAES-*co*-$(PEG100)_2$ and PAES-*co*-$(ZW40/PEG60)_2$ membranes did not undergo any dimensional change with 100% retention resulting from the robust thermal stability of the PAES regions. The DSC and TGA analyses, along with thermal shrinkage tests, reveal that the PAES-*co*-$(PEG100)_2$ and PAES-*co*-$(ZW40/PEG60)_2$ membranes offer both substantial mechanical strength and excellent thermal stability, fulfilling essential criteria for solid electrolytes in LSBs.

The flame-retardant behavior of solid electrolyte fundamentally influences the safety and long-term reliability of the battery. A high flame-retardant solid electrolyte can significantly reduce the risk of fire or explosion in cases of internal short circuits or overcharging and enhance the safety of the battery during operation, especially in high-temperature environments. Consequently, the flame-retardant test was conducted on PAES-*co*-$(PEG100)_2$ and PAES-*co*-$(ZW40/PEG60)_2$ membranes using a direct alcohol lamp, with the outcomes compared to those of a commercial PP separator fully immersed in 1 M $LiPF_6$ solution prepared with DEC/PC/EC mixed at a 1 : 1 : 1 volume ratio, as depicted in Fig. S10. Both PAES-*co*-$(PEG100)_2$ and PAES-*co*-$(ZW40/PEG60)_2$ membranes cannot be ignited upon exposure to the flame, and they self-extinguish once removed from the flame due to good non-flammability of IL and PAES. In contrast, the commercial PP separator exhibited rapid burning upon exposure to the flame. This result indicated that all synthesized membranes are promising for enhancing the safety performance of LSBs.

Electrochemical and interfacial stabilities

Another critical factor is the electrochemical potential window, ensuring that the solid electrolyte does not decompose into harmful products during operation of LSBs. A wide and stable electrochemical window enables higher energy densities, longer cycle lives, and safer operation across a variety of applications. Therefore, the electrochemical stability window of PAES-*co*-$(PEG100)_2$ and PAES-*co*-$(ZW40/PEG60)_2$ membranes was determined by the linear sweep voltammogram (LSV) test. Fig. 4a (inset) reveals that the PAES-*co*-$(ZW40/PEG60)_2$ membrane displayed minor anodic current (<0.2 mA cm^2) with an electrochemical stability limit of 5.28 V. In contrast, the LSV profiles of the PAES-*co*-$(PEG100)_2$ membrane exhibited a significant increase in anodic currents upon reaching 5.01 V. The enhancement of the potential window in the PAES-*co*-$(ZW40/PEG60)_2$ membrane is attributed to the presence of ZW segments containing fluorinated anionic (Tf_2N^-) sites, which facilitate the delocalization of negative charges. The delocalization of negative charges over the Tf_2N^- sites within the ZW segments reduces the charge density on individual atoms, thereby decreasing the reactivity of the anion, which stabilizes it against oxidative or reductive decomposition. This stabilization minimizes the likelihood of the anion participating in unwanted side reactions, such as nucleophilic attacks or reduction at the electrode surface. Hence, the membrane is capable of operating over a wider voltage range without degradation, thereby enhancing the electrochemical stability window. Consequently, the prepared PAES-*co*-$(ZW/PEG)_2$ membrane exhibits sufficient electrochemical stability as a solid polymer electrolyte, making it suitable for applications not only in LSBs but also in high-voltage LIBs.

Interfacial stability is crucial in lithium-based batteries because it directly affects the battery's performance, safety, and lifespan. At the junction of the solid electrolyte and the electrode, unstable interfaces can lead to electrolyte decomposition, resulting in the formation of unwanted by-products. This degradation not only reduces battery efficiency but also consumes active lithium, leading to capacity fade. The characteristics of the Li-electrode/solid electrolyte interface are largely influenced by the structural characteristics and composition of the salt anion, both during storage and operation. Therefore, the interfacial stability of PAES-*co*-$(PEG100)_2$ and PAES-*co*-$(ZW40/PEG60)_2$ membranes is comparatively evaluated by examining the change in interface resistance over different storage times and the establishment of the interfacial layer (SEI) under working conditions using lithium plating/stripping measurements. Symmetric PAES-*co*-$(PEG100)_2$ and PAES-*co*-

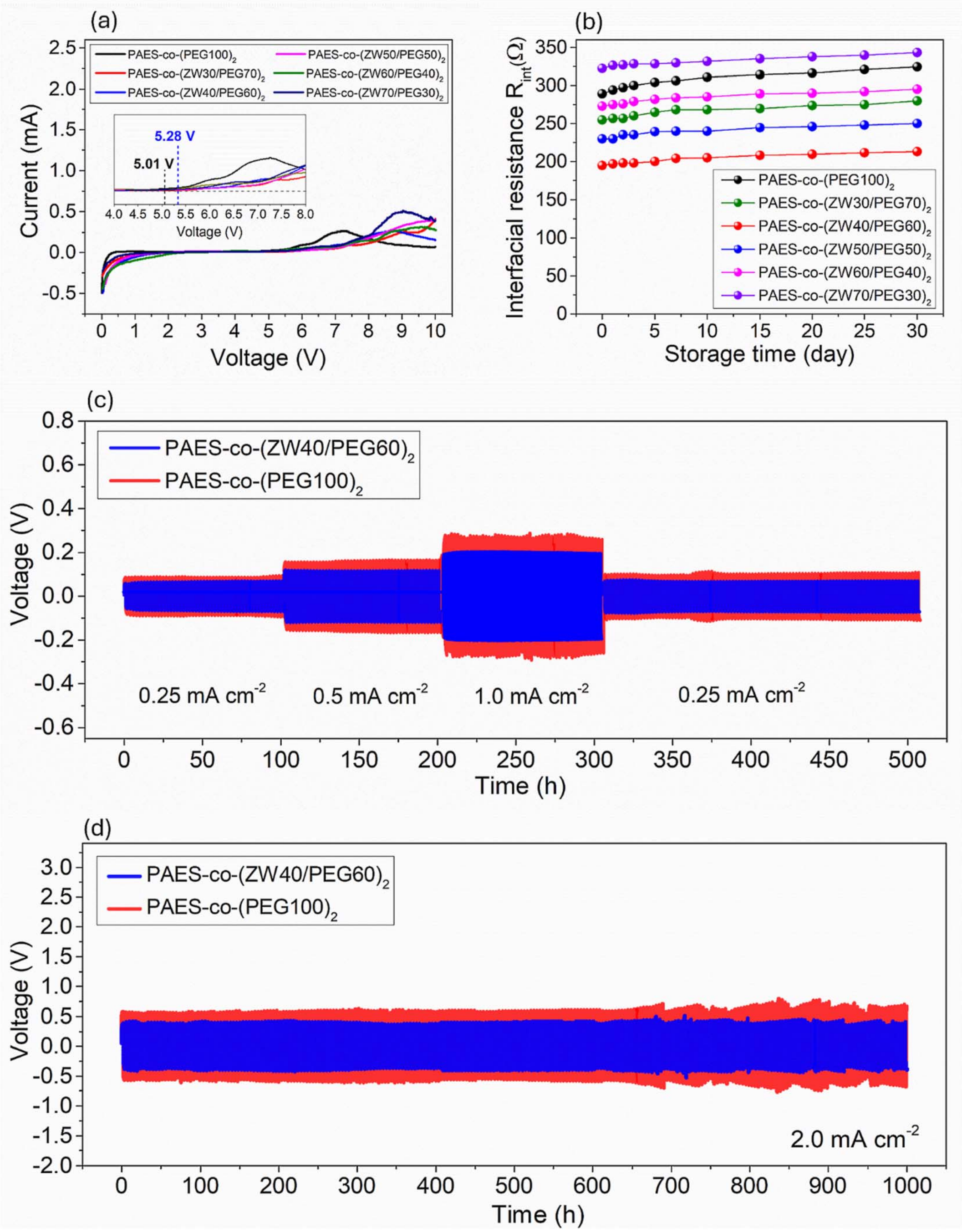

Fig. 4 (a) LSV curves; (b) relationship between interfacial resistance and storage time; (c) lithium stripping/plating test at various current densities; and (d) lithium stripping/plating test at 2.0 mA cm^{-2} during 1000 h of cycling of cells assembled with PAES-*co*-(PEG100)$_2$ and PAES-*co*-(ZW40/PEG60)$_2$ membranes containing 70 wt% IL–EC contents.

(ZW40/PEG60)$_2$ cells were analyzed by EIS after resting them at 30 °C for various time spans. The temporal variation of R_i derived from EIS analysis for PAES-*co*-(PEG)$_2$ and PAES-*co*-(ZW40/PEG60)$_2$ membranes is illustrated in Fig. 4b. The freshly assembled symmetric Li cell exhibits a lower initial R_i for PAES-*co*-(ZW40/PEG60)$_2$ (195 Ω) compared to PAES-*co*-(PEG100)$_2$ (289 Ω) on day 0. After 5 days of storage, both electrolytes show minor temporal variations in R_i, culminating at 304 Ω for PAES-*co*-(PEG100)$_2$ and 200 Ω for PAES-*co*-(ZW40/PEG60)$_2$, respectively, reflecting ongoing SEI formation and reconstruction. Upon extended storage, the nearly unchanged R_i values of PAES-*co*-(ZW40/PEG60)$_2$ (205 Ω on day 10 and 213 Ω on day 30) demonstrate excellent Li electrode–electrolyte interfacial stability. By contrast, the R_i of PAES-*co*-(PEG100)$_2$ slightly increases from 311 Ω (day 10) to 324 Ω (day 30). These results clearly demonstrate that the interface between the Li electrode and PAES-*co*-(ZW40/PEG60)$_2$ is more stable than that between the Li electrode and PAES-*co*-(PEG100)$_2$. Compared with other

PAES-*co*-(ZW/PEG)$_2$ membranes at different ZW/PEG ratios, no significant difference is observed in the overall trend of interfacial resistance evolution with storage time. All PAES-*co*-(ZW/PEG)$_2$ membranes show a gradual increase in interfacial resistance during storage, which is attributed to the formation and stabilization of the solid electrolyte interphase. Notably, as the ZW/PEG ratio increases from 30 : 70 to 70 : 30, the increment in interfacial resistance with storage time becomes smaller (from approximately a 10 to 7% increment after 30 days). This behavior can be attributed to the higher density of zwitterionic groups, which enhances interfacial chemical stability and suppresses spontaneous side reactions at the Li metal interface, thereby leading to a more stable and less resistive interphase. Despite the incomplete understanding of the mechanism for stable SEI layer formation in LiTf$_2$N/PEG, the structural modification through ZW/PEG co-grafting significantly contributes to the enhanced interfacial stability of Li/SPE in PAES-*co*-(ZW40/PEG60)$_2$.

The electrolyte–Li metal anode interfacial stability was further evaluated through lithium plating/stripping tests on symmetric Li–Li cells containing PAES-*co*-(PEG100)$_2$ and PAES-*co*-(ZW40/PEG60)$_2$. As shown in the voltage profiles of Li plating/stripping in Fig. 4c, when the operation of the PAES-*co*-(ZW40/PEG60)$_2$ cell is conducted at 0.25 mA cm^{-2}, the overpotential reaches 80 mV, which is smaller than that of the PAES-*co*-(PEG100)$_2$ cell (100 mV) during the first 100 h. Upon increasing current density, the PAES-*co*-(ZW40/PEG60)$_2$ cell exhibits only a slight increase in overpotential with 120 and 195 mV for 0.5 and 1.0 mA cm^{-2}, which remains significantly lower than the overpotentials observed in the PAES-*co*-(PEG100)$_2$ cell (165 and 290 mV). Even after reverting to 0.25 mA cm^{-2}, the PAES-*co*-(ZW40/PEG60)$_2$ cell displays only 90 mV overpotential, representing a 12.5% increase. In contrast, the PAES-*co*-(PEG100)$_2$ cell shows a greater increase in overpotential (120 mV) with a 20% rise. This enhanced performance is ascribed to the development of a more robust SEI layer, resulting from superior ionic conductivity coupled with Li-ion transference characteristics (t_{Li^+}) of PAES-*co*-(ZW40/PEG60)$_2$ compared to PAES-*co*-(PEG100)$_2$.

Conversely, the Li anode-membrane interfacial stability under dynamic conditions was also evaluated through polarization testing of the symmetric battery over an extended period (Fig. 4d). Both symmetric PAES-*co*-(ZW40/PEG60)$_2$ and PAES-*co*-(PEG100)$_2$ cells underwent repeated charge–discharge cycles upon applying 2.0 mA cm^{-2} for 0.5 hours per half-cycle. The PAES-*co*-(ZW40/PEG60)$_2$ cell retained a low voltage polarization (only increased 8% of 480 mV initial overpotential) with no short-circuit failure after 1000 hours of cycling, indicating high stability for lithium plating and stripping within the battery (refer to Fig. 4d). In contrast, the PAES-*co*-(PEG100)$_2$ cell exhibited higher voltage polarization (710 mV), with an increment of 14% after 1000 cycles. For further insight into the electrochemical performance, post-cycling SEM characterization of the Li–electrolyte interface (Fig. S11) reveals that, with PAES-*co*-(ZW40/PEG60)$_2$, the Li surface retained a smooth and dense morphology, comparable to its pre-cycling state. Meanwhile, the cell using the PAES-*co*-(PEG100)$_2$ membrane resulted in a rough Li surface, characterized by white spots indicative of an increased presence of "dead" or isolated lithium. These findings suggest that the PAES-*co*-(ZW40/PEG60)$_2$ cell exhibits improved interfacial compatibility with the Li-anode during repeated lithium electrode cycling, which prevents the propagation of Li dendrites and results in a smooth lithium surface through the co-grafting of PEG and ZW. This co-grafting promotes rapid single Li-ion transport not only within the membrane but also across the membrane/Li anode interface. This result is further supported by the slight variation in interfacial resistance (R_{i}) of the PAES-*co*-(ZW40/PEG60)$_2$ cell before and after 1000 hours of cycling. As shown in Fig. S12, the R_{i} for the PAES-*co*-(ZW40/PEG60)$_2$ cell was ~198 Ω, representing a 21% increase, significantly lower than the ~378 Ω (39% increase) observed for the PAES-*co*-(PEG100)$_2$ cell. This observation suggests that propagation of Li dendrites within the PAES-*co*-(ZW40/PEG60)$_2$ cell is mitigated through the stable SEI layer establishment, along with selective Li-cation conduction arising from the confinement of Tf$_2$N$^-$ anions through repulsive interactions with PYR-cationic sites in the ZW moiety. Moreover, Li-ion transport was facilitated through interactions with anionic sites in the ZW segment, aided by EC additives and the segmental motion of PEG. The co-grafting of PEG and ZW onto the PAES backbone, which effectively inhibits Li dendrite formation, provides a viable strategy to improve the cycling stability of LSBs.

Suppression of polysulfide shuttle

Suppressing the polysulfide shuttle is key to unlocking the full potential of LSBs by improving capacity retention, coulombic efficiency, and cycle life and reducing self-discharge. Polysulfide, generated from electrochemical reactions at the cathode during charge and discharge, can be diffused to the anode through electrolyte and causes unwanted side reactions at the anode, leading to a continuous consumption of lithium and electrolyte and a decrease in the specific capacity and coulombic efficiency. To examine polysulfide regulation, the PAES-*co*-(ZW40/PEG60)$_2$ and PAES-*co*-(PEG100)$_2$ membranes underwent visualization of polysulfide diffusion. In an H-type cell, the prepared membranes were used to separate a 0.4 M Li$_2$S$_4$ solution (DOX/DME/MeCN) from the blank solvent (Fig. 5a). With PAES-*co*-(PEG100)$_2$, a distinct color transition from colorless to light yellow at 16 h and further to dark yellow at 48 h was observed in the opposite chamber, demonstrating the diffusion of polysulfide species and the resulting severe polysulfide shuttling in LSBs. On the other hand, the as-synthesized PAES-*co*-(ZW40/PEG60)$_2$ membrane preserved a colorless and transparent solution up to 16 h, subsequently turning light yellow after 24 h. Based on the UV-vis measurements (Fig. S13), the PAES-*co*-(ZW40/PEG60)$_2$ membrane with a PS permeability of ~3.418 × 10–5 cm^2 s^{-1} exhibited a markedly lower value than the PAES-*co*-(PEG100)$_2$ membrane (6.601 × 10^{-5} cm^2 s^{-1}) demonstrating its superior ability to suppress polysulfide migration (see Fig. 5b). In comparison, the PAES-*co*-(ZW40/PEG60)$_2$ membrane demonstrated a significantly superior polysulfide (PS) shuttle inhibition than that reported in previous studies as described in Fig. 6c.[61–69] This excellent polysulfide obstruction of the PAES-*co*-(ZW40/PEG60)$_2$ membrane originates from the strong ZW–LiPS interactions, forming PYR$^+$/PS$^-$ and Tf$_2$N$^-$/Li$^+$ couples, consistent with electrostatic and Lewis acid–base interaction mechanisms (as illustrated in Fig. 5d). The XPS test was also conducted to analyze the interaction between PS and the prepared membranes (PAES-*co*-(PEG100)$_2$ and PAES-*co*-(ZW40/PEG60)$_2$). In the S 2p XPS spectra of these tested membranes, the PYR$^+$/PS$^-$ interactions appear at 164.4 eV as depicted in Fig. S14. Such interactions firmly immobilize initially leached polysulfides, establishing a concentration gradient barrier hindering further polysulfide diffusion, while promoting favorable Li-ion transport. This property contributes to effective suppression of polysulfide shuttling and improved LSB stability.

Lithium-based secondary battery performance

Application in lithium sulfur batteries. To examine their electrochemical behavior, the prepared membranes were tested in LSB cells prepared from a Li-anode with a thickness of 0.15 mm and an S cathode with a loading amount of 5.6 mg cm^{-2} on aluminium foil. The CV profiles of PAES-*co*-(ZW40/PEG60)$_2$ and PAES-*co*-(PEG100)$_2$ cells, recorded at scan rates ranging from 0.2–0.5 mV s^{-1}, are shown in Fig. 6a and b. Generally, two broad peaks appear in both cells, reflecting the sequential two-step sulfur reduction in the cathodic scan (2.8–1.5 V). The first peak (~2.25 V, peak C$_2$) corresponds to S reduction to Li$_2$S$_n$ (n = 4–8), while the second peak (~1.90 V, peak C$_1$) represents further reduction to lithium sulfide (Li$_2$S$_2$

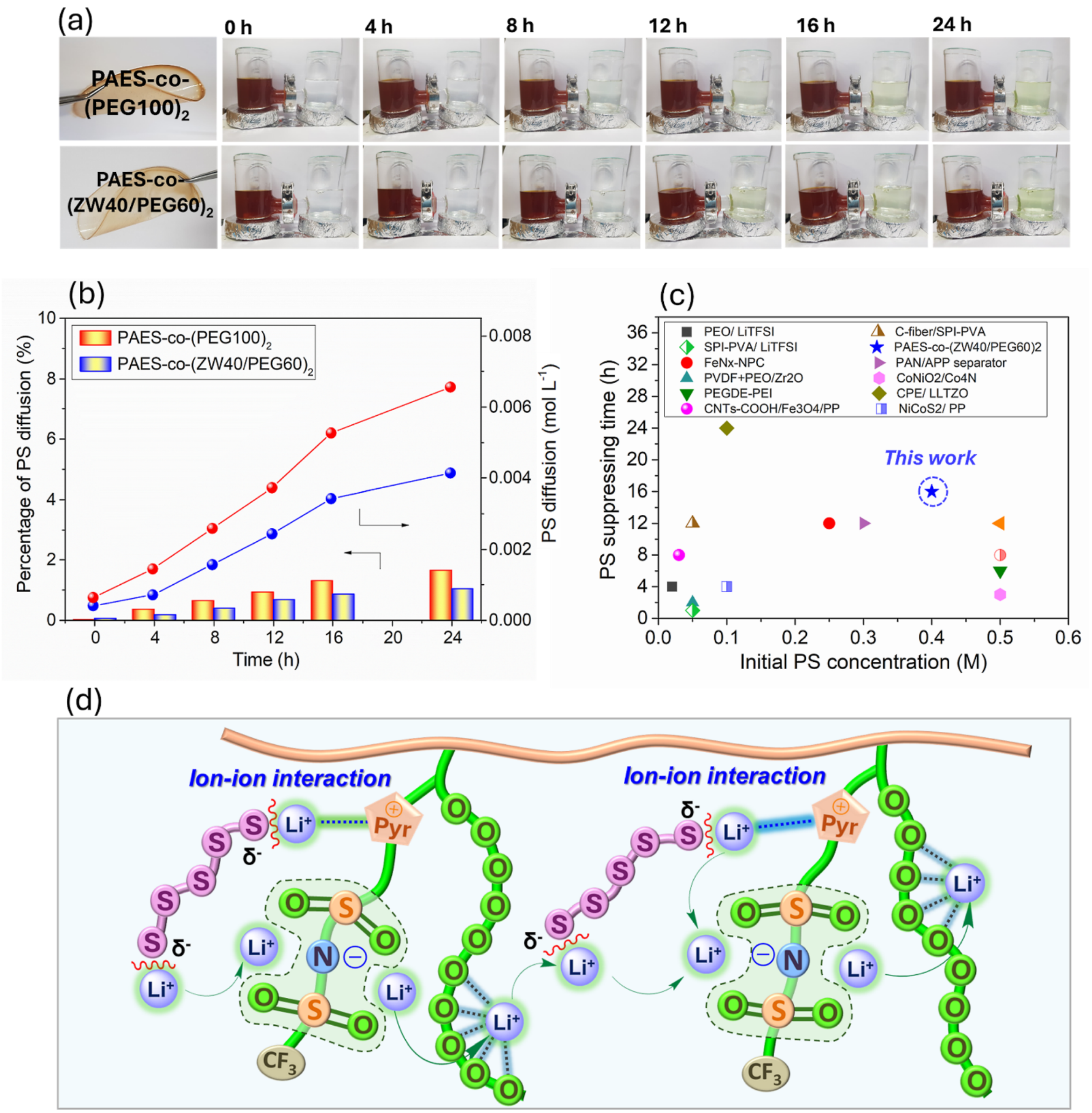

Fig. 5 (a) Optical images of the PS permeability test; (b) PS permeability of PAES-*co*-(PEG100)$_2$ and PAES-*co*-(ZW40/PEG60)$_2$ membranes containing 70 wt% IL–EC contents; (c) comparison of suppression of PS diffusion of the PAES-*co*-(ZW40/PEG60)$_2$ membrane with that of other solid electrolytes; and (d) illustration of diffusing PS suppression of the PAES-*co*-(ZW40/PEG60)$_2$ membrane under the effect of ZW graft chains.

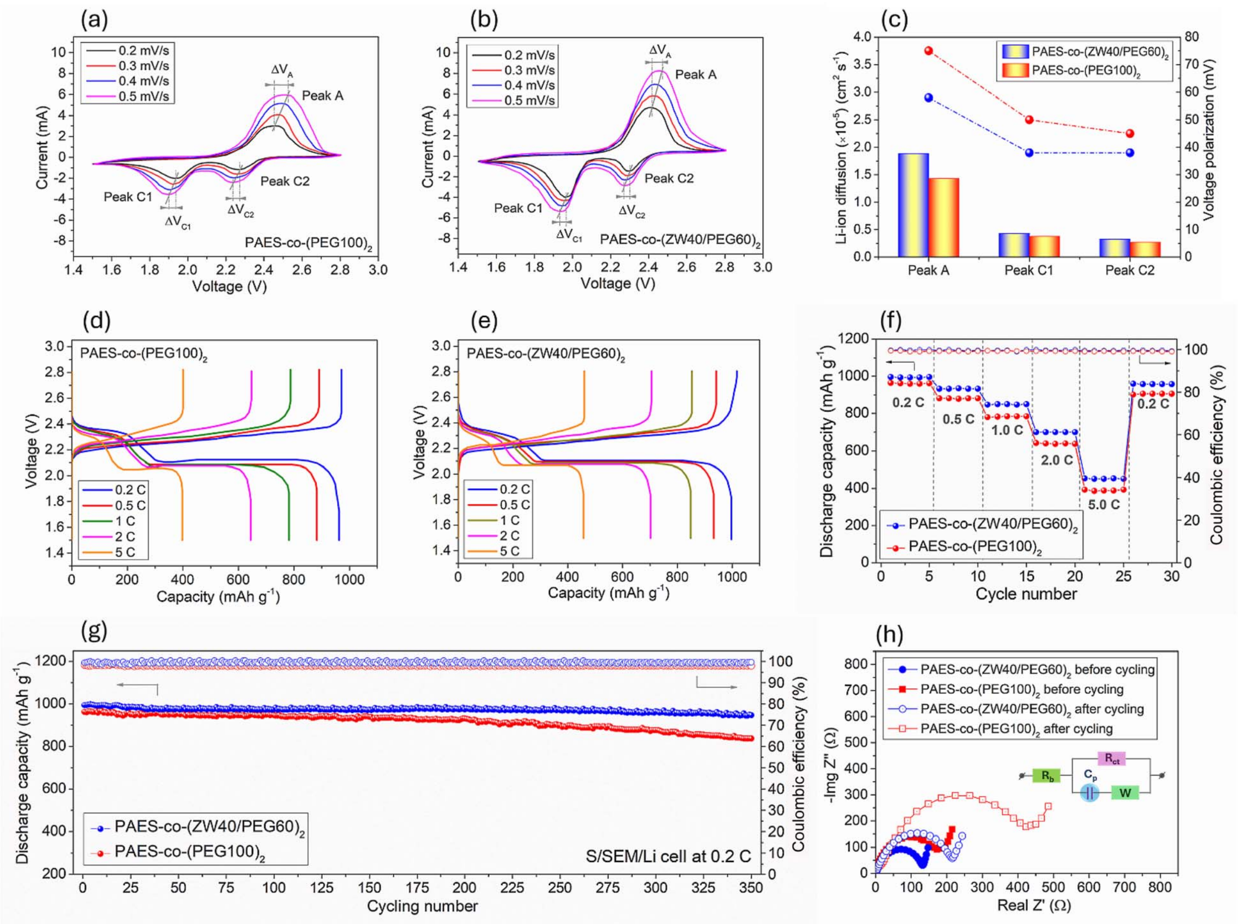

Fig. 6 (a and b) CV curves at various scan rates; (c) Li-ion diffusion and polarization; (d and e) charge–discharge profiles; (f) rate capability; (g) cycling performance; and (h) interfacial resistance before and after 350 cycles of the S/SEM/Li cell assembled with PAES-*co*-(PEG100)$_2$ and PAES-*co*-(ZW40/PEG60)$_2$ membranes containing 70 wt% IL–EC contents.

and Li_2S). The reverse scan exhibits a broad anodic peak (peak A) at ~2.42 V, associated with the reoxidation to Li_2S_8/S_8. Lithium cation diffusivity ($D_{\text{Li-cation}}$) values were extracted from the I–$\nu^{0.5}$ plot according to the Randles–Sevcik model (Fig. S15). The calculated $D_{\text{Li-cation}}$ and polarization (ΔV) of both PAES-*co*-(ZW40/PEG60)$_2$ and PAES-*co*-(PEG100)$_2$ were compared and are shown in Fig. 6c. The PAES-*co*-(ZW40/PEG60)$_2$ cell has much higher lithium cation diffusivity (0.429×10^{-5} (peak C_1), 0.327×10^{-5} (peak C_2), and 1.88×10^{-5} cm^2 s^{-1} (peak A)) when compared to the PAES-*co*-(PEG)2 cell (2.747×10^{-5} (peak C_1), 0.989×10^{-5} (peak C_2), and 3.205×10^{-5} cm^2 s^{-1} (peak A)). Besides, GITT measurements were performed to evaluate the Li^+ diffusion behavior of sulfur cathodes using PAES-*co*-(PEG100)$_2$ and/or PAES-*co*-(ZW40/PEG60)$_2$. Both cells were tested in the voltage range of 1.5–2.8 V (*vs.* Li^+/Li) at a constant current rate of 0.2 C, applying a 5 min current pulse followed by a 1 h relaxation period to approach equilibrium. The GITT curves and Li-ion diffusion coefficients ($D_{\text{Li-ion}}$) of both cells are presented in Fig. S16. Here, the GITT voltage profiles show that the PAES-*co*-(ZW40/PEG60)$_2$ cell exhibits smaller polarization (ΔE_τ) and faster voltage relaxation than the PAES-*co*-(PEG100)$_2$ cell throughout the discharge process, indicating reduced internal resistance and improved Li-ion transport kinetics (see Fig. S16a and b). Based on the Weppner–Huggins equation, the $D_{\text{Li-ion}}$ values were calculated at different voltages and are summarized in Fig. S16c. The PAES-*co*-(ZW40/PEG60)$_2$ cell consistently shows higher $D_{\text{Li-ion}}$ values over the entire voltage range. This enhancement is attributed to the zwitterionic groups, which facilitate Li^+ dissociation and transport within the sulfur composite electrode. These results suggest that the Li-ion migration kinetics of the PAES-*co*-(ZW40/PEG60)$_2$ cell are markedly improved because of the efficient Li-ion migration within the cathode binder phase and quasi-solid electrolyte matrix due to the synergistic effect of co-grafting PEG and ZW. Fig. 6d and e illustrate the first-cycle voltage profiles during charge and discharge for the PAES-*co*-(ZW40/PEG60)$_2$ and PAES-*co*-(PEG100)$_2$ cells operated at various C rates. Lower polarization was observed in the PAES-*co*-(ZW40/PEG60)$_2$ cell compared to the PAES-*co*-(PEG100)$_2$ cell, in agreement with the CV measurements. The highly effective Li-ion migration within the quasi-solid electrolyte likely accounts for the low polarization behavior of the PAES-*co*-(ZW40/PEG60)$_2$ cell. Fig. 6f compares the rate capabilities of the PAES-*co*-(ZW40/PEG60)$_2$ and PAES-*co*-(PEG100)$_2$ cells in more detail. The PAES-*co*-(ZW/PEG)$_2$ cell delivers reasonable discharge capacities of 995.5 (0.2 C), 933.2 (0.5 C), 848.2 (1.0 C), 700.3 (2.0 C) and 452.3 mAh g^{-1} (5.0 C). Upon reverting the cycling rate to 0.2 C, the cell recovers 959.5 mAh g^{-1} discharge capacity, corresponding to 96% of its baseline capacity prior to subjecting the cell to high C-rate conditions. Furthermore, the delivered capacities remain nearly constant over five cycles at each C-rate. In contrast, the PAES-*co*-$(PEG100)_2$ cell has lower discharge capacity at each C rate, with more pronounced capacity fading at higher cycling rates, retaining only 93% of its initial capacity prior to undergoing high C-rate cycling. The benefits of using PAES-*co*-$(ZW40/PEG60)_2$ are obvious from the above comparison between its cell and the PAES-*co*-$(PEG100)_2$ cell. Long-term cycling characteristics of the PAES-*co*-$(ZW40/PEG60)_2$ and PAES-*co*-$(PEG100)_2$ cells are also investigated at 0.2 C and compared in Fig. 6g. The PAES-*co*-$(PEG100)_2$ cell experiences a significant reduction in discharge capacity, retaining 937.1 mAh g^{-1}, equivalent to 86% retention over 350 cycles. This outcome mainly originates from the low Li-ion conductivity (see Fig. 2) and polysulfide shuttling from the cathode to the anode (Fig. 5) over extended cycling. Interactions of the migrated polysulfides with the lithium anode induce depletion of active sulfur and passivation of the surface, thereby decreasing coulombic efficiency and limiting battery longevity. In contrast, PAES-*co*-$(ZW40/PEG60)_2$ effectively confines polysulfides within the cathode and enables efficient Li-ion transport in the quasi-solid electrolyte due to the synergistic effect of co-grafting PEG and ZW segments. As a result, the PAES-*co*-$(ZW40/PEG60)_2$ cell demonstrates prolonged cycling stability and remarkable retention of discharge capacity. Across 350 cycles, the PAES-*co*-$(ZW40/PEG60)_2$ cell retains 93% of its initial capacity, with a minimal rate of capacity loss of only 0.02% per cycle. Additionally, a high and stable coulombic efficiency is retained by the PAES-*co*-$(ZW40/PEG60)_2$ cell over the 350 cycles, attaining 99.1% at cycle 350). In particular, the PAES-*co*-$(ZW40/PEG60)_2$ cell was still stable at 2.0 C, delivering 556.5 mAh g^{-1} (79% of initial discharge capacity) after the 200th cycle with 99.2% coulombic efficiency (see Fig. S17). Fig. 6i shows that the overall resistance of the PAES-*co*-$(ZW40/PEG60)_2$ cell slightly increases from 130 Ω at the initial state to 200 Ω after the 350th cycle, while the PAES-*co*-$(PEG100)_2$ cell has a big increment in interfacial resistance (from 170 Ω to 410 Ω). The pronounced resistance growth is mainly attributed to the formation of LiF on the lithium metal surface, as confirmed by SEM and XPS analysis (Fig. S18 and S19). The generation of LiF originates from the electrochemical decomposition of F-containing electrolyte components and Li salt at the Li interface under repeated cycling, leading to the accumulation of an insulating LiF-rich interphase that impedes Li-ion transport. Moreover, the post-cycling morphology and elemental distribution of the sulfur cathodes were examined by SEM and EDS, as shown in Fig. S20. The PAES-*co*-$(PEG)_2$ cathode exhibits a relatively rough and heterogeneous surface after cycling, together with a less uniform sulfur distribution. EDS analysis shows a sulfur content of 19.07 wt%, indicating partial sulfur loss and nonuniform sulfur redeposition during repeated cycling. In contrast, the PAES-*co*-$(ZW40/PEG60)_2$ cathode exhibits a more compact and homogeneous morphology. A higher sulfur content of 21.91 wt% is detected, accompanied by uniform sulfur mapping across the electrode. Moreover, the presence of a well-distributed nitrogen signal confirms the successful incorporation of ZW groups. These ZW functionalities effectively anchor lithium polysulfides and suppress their dissolution, thereby preserving the cathode structure and enhancing sulfur retention after cycling. These results clearly imply the high interfacial compatibility between the electrode and PAES-*co*-$(ZW40/PEG60)_2$ membrane due to its excellent Li-ion transport characteristics (σ = 1.58 mS cm^{-1}; t_{Li^+} = 0.752) together with effective suppression of polysulfide migration (P_{PS} = 6.601 × 10^{-5} cm^2 s^{-1}). As far as we are aware, the PAES-*co*-$(ZW40/PEG60)_2$ cell's electrochemical performance was evaluated relative to recently reported Li–S cells incorporating different solid electrolytes. Table S3 highlights the superior electrochemical performance of the PAES-*co*-$(ZW/PEG)_2$ cell.

Performance evaluation in high-voltage Li-ion batteries. Coin cells were assembled with a $LiNi_{0.5}Mn_{1.5}O_4$ (LNMO) cathode and Li-anode to characterize the electrochemical performance of the PAES-*co*-$(ZW40/PEG)_2$ membrane for high voltage Li-ion battery application. As shown in Fig. 7(a and b), the PAES-*co*-$(ZW40/PEG60)_2$ cell was charged and discharged to 4.9 V at 0.2 C, achieving 120.4 mAh g^{-1} first-cycle capacity together with 99.7% CE, which is higher than that of the PAES-*co*-$(PEG100)_2$ cell (115.4 mAh g^{-1} first-cycle capacity along with 99.6% CE). Fig. 7c shows rate performance of the PAES-*co*-$(PEG100)_2$ and PAES-*co*-$(ZW40/PEG60)_2$ cells subjected to C-rates spanning 0.2–2.0 C. The PAES-*co*-$(ZW40/PEG60)_2$ cell attained average specific capacities of 120.4 (0.2 C), 115.2 (0.5 C), 102.1 (1.0 C), and 78.6 mAh g^{-1} (2.0 C). Upon reverting the C-rate to 0.2 C, 117.4 mAh g^{-1} average capacity was recovered with 97.5% rate capability, demonstrating excellent cycling stability and reversible performance. Conversely, the PAES-*co*-$(PEG100)_2$ cell achieved substantially reduced discharge capacities (115.4, 107.8, 91.6, and 67.2 mAh g^{-1}) under identical C-rate conditions and low rate capability (94.3%) after returning to 0.2C. The good cycling stability of the PAES-*co*-$(ZW40/PEG60)_2$ cell was also evaluated at 0.2 C through a long term cycling performance test (Fig. 7d). The capacity retention of the PAES-*co*-$(ZW40/PEG60)_2$ cell is 96% with a coulombic efficiency of 99.5%, which is higher than that of the PAES-*co*-$(PEG100)_2$ cell (92% capacity retention and a CE of 99.4%) after the 200th cycle. Furthermore, EIS analyses were performed on the cells at ambient temperature both prior to and following 200 cycles (Fig. 7e). In the Nyquist spectra, the real-axis intercept at high frequencies indicates the resistance of the electrolyte membrane and the cathodic SEI, and the semicircles in the mid-frequency range correspond to interfacial charge-transfer processes. The interfacial resistance of the PAES-*co*-$(ZW40/PEG60)_2$ cell was measured to be 167.8 and 211.95 Ω cm^{-2} before and after 200 cycles, respectively, indicating a smaller increase and overall lower resistance compared to the PAES-*co*-$(PEG100)_2$ cell (220.8 and 309.1 Ω cm^{-2}). This finding suggests that the PAES-*co*-$(ZW40/PEG60)_2$ cell exhibits superior cycling stability under high-voltage conditions. The enhanced electrochemical performance of the PAES-*co*-$(ZW40/PEG60)_2$ cell is primarily governed by two key mechanisms. First, the incorporation of PEG not only improved the electrolyte–lithium interface (Fig. 4) but also likely facilitated superior electrolyte–cathode

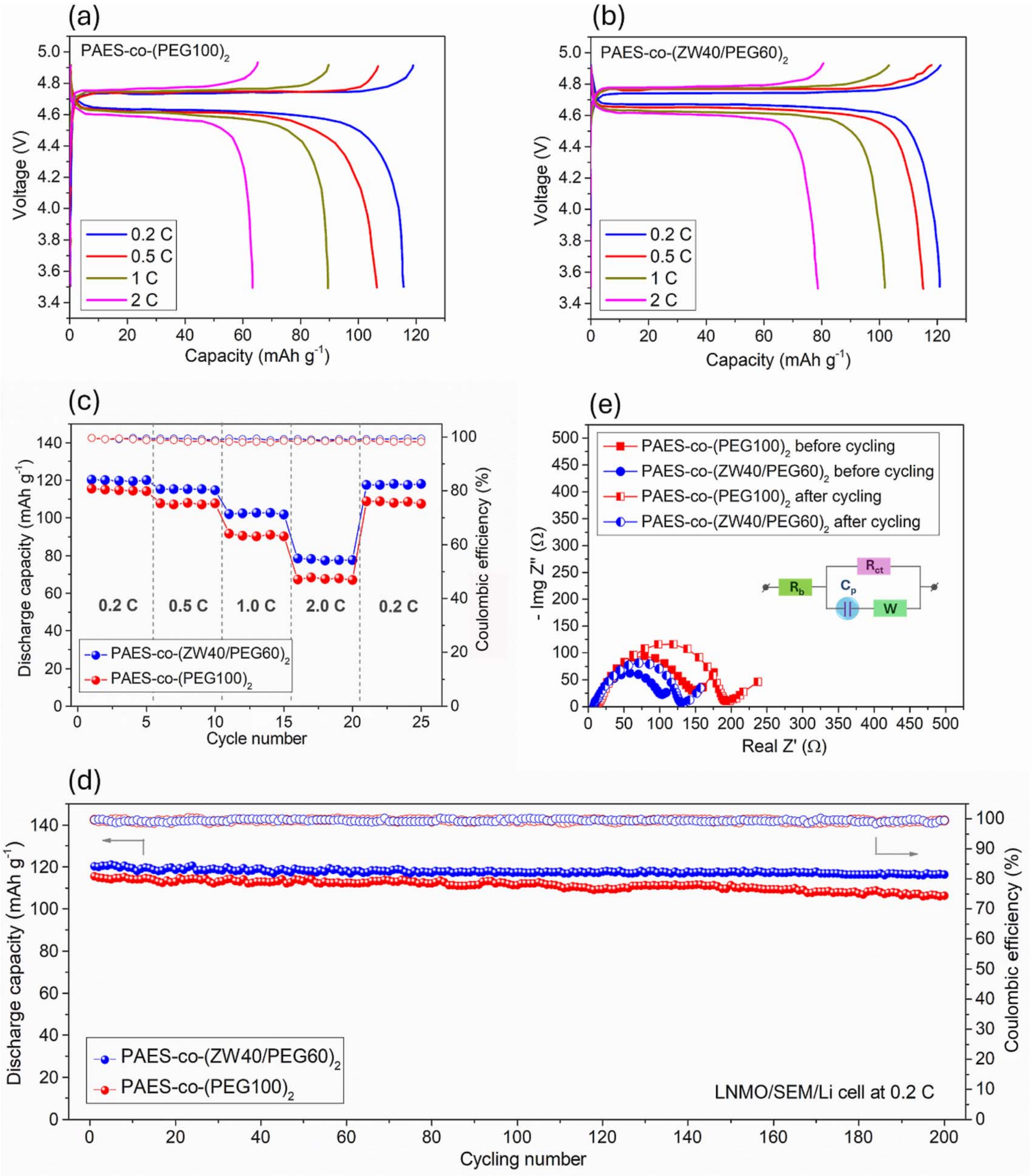

Fig. 7 (a and b) Charge–discharge profiles; (c) rate capability; (d) interfacial resistance; and (f) cycling performance at a 0.2 C-rate in a voltage range from 4.9 to 3.5 V of the LNMO/SEM/Li cell assembled with PAES-*co*-(PEG100)$_2$ and PAES-*co*-(ZW40/PEG60)$_2$ membranes containing 70 wt% IL–EC contents.

contact, thereby inducing depolarization effects and significantly enhancing LIB performance. Second, the reduced overpotential indicates lower internal resistance and improved ion transport capability of the membrane, which is consistent with the data in Fig. 2, where PAES-*co*-(ZW/PEG)$_2$ demonstrated the highest ionic conductivity.

Experimental

Materials

Lithium bis(fluoromethanesulfonyl) imide (LiTf$_2$N), acetylacetate, ethylene carbonate (EC), 1-iodobutane (IB), and *N*-methylpyrrolidine were obtained from Sigma-Aldrich (Milwaukee, WI, USA) and used for the preparation of the IL–EC mixture. All organic solvents such as propan-2-ol (IPA, 99.0%), methanol, *N*,*N*-dimethylformamide (DMF, 99.0%), toluene, dichloromethane (DCM), 1-methyl-2-pyrrolidone (anhydrous NMP, >99.0%), acetonitrile (MeCN), and tetrahydrofuran (THF, 99.0%) were provided by Samchun Pure Chemical company (Seoul, Republic of Korea). Potassium carbonate (K2CO3), 4-dimethylaminopyridine, *N*,*N*′-dicyclohexylcarbodiimide, hydrochloric acid (HCl, 35.0–37.0%), bis(4-fluorophenyl) sulfone, diphenolic acid, dimethyl sulfoxide (DMSO, 99.0%), and *cis*-butenedioic acid were supplied by Junsei Chemical Co., Ltd

(Japan) for PAES-2COOH preparation (two carboxyl pendant groups). Both pyridine and chloroform were dehydrated over 4 Å Linde molecular sieves. *P*-toluenesulfonyl chloride, iodotrimethylsilane, 1-bromobutane (98.5%), and pyrrolidine (99%) were received from Tokyo Chemical Industry (TCI, Japan). For cathode preparation, both electrically conductive graphite and cathodic sulfur (S) were also purchased from the MTI Korea company (Seoul, Republic of Korea).

Preparation of *N*-(((3-[1-(11-hydroxyundecyl) pyrrolidinium)] propyl) sulfonyl) trifluoromethanesulfonyl)-imide (ZW)

A mixture solution of 1-(11′-hydroxyundecyl) pyrrolidine (7.4 g, 0.030 mol) and potassium (3-chloropropylsulfonyl) (trifluoromethyl-sulfonyl) imide (5.0 g, 0.015 mol) in acetonitrile (10 mL) was refluxed for 4 days. Following the cooling of the mixture to ambient temperature, rotary evaporation was employed to remove the solvent. The residual solid was dissolved in acetonitrile and purified by sequential reprecipitation, initially using diethyl ether, followed by deionized water. The filtrate was subsequently dried under vacuum, resulting in a crystalline solid (6.2 g, 82%). DSC: $T_m = 68$ °C (1st heating).

^{1}H-NMR (ZW) (500 MHz, 23 °C DMSO-d_6, δ) 1.25 (m, 14H), 1.39 (m, 2H), 1.63 (m, 2H), 2.04 (m, 6H), 3.08 (t, $J = 7$, 2H), 3.22 (m, 2H), 3.35 (m, 2H), 3.47 (m, 4H), 4.34 (t, $J = 5$, 1H).

Poly(arylene ether sulfone) with dual carboxylic acid groups (PAES-2COOH)

First, bis(4-fluorophenyl) sulfone (0.03 mol) and diphenolic acid (0.03 mol) were used to synthesize the PAES backbone as introduced in the Experimental section in the SI. The pre-prepared PAES (7.66 g), maleic acid (3.02 g), and 4-dimethylaminopyridine (0.21 g) were diluted in DMF (100 mL) solvent and continuously stirred at 80 °C within a three-necked round-bottom flask (500 mL capacity) to ensure complete solution uniformity. A DMF solution (5 mL) containing *N*,*N*′-dicyclohexylcarbodiimide (3.93 g) was gradually introduced to minimize side reactions. The reactor was heated and stirred for 6 h at 90 °C under a nitrogen atmosphere. After 3 d, the mixture was permitted to reach ambient temperature and filtered using filter paper to eliminate some small white solids. The solution was slowly dropped in 150 mL of propan-2-ol to isolate PAES-2COOH as a solid. Afterward, these filtered solids were washed twice with deionized water (pH = 5.5) and dried in an oven at 75 °C for 2 d to eliminate water (yielding ∼85%).

Preparation of PAES-*co*-(ZW/PEG)$_2$

PAES-*co*-(ZW/PEG)$_2$ was prepared by esterification of PAES-2COOH with PEG (see Fig. S1). This reaction was implemented at 80 °C in a three-necked laboratory glass vessel (250 mL capacity) and *N*,*N*′-dicyclohexylcarbodiimide (2.06 g), PEG (11.0 g), PAES-2COOH (2.64 g), and 4-dimethylaminopyridine (0.029 g) were introduced together with DMF (70 mL). The mixture was maintained to facilitate the reaction for 48 h and then precipitated into 50 mL of diethyl ether to get small white solids and they were twice purified with deionized water. The PAES-*co*-(ZW/PEG)$_2$ solids were dried overnight at 80 °C in a vacuum oven (affording a 70% yield).

^{1}H-NMR (DMSO-d_6, 500 MHz) (PAES-*co*-(ZW/PEG)$_2$): 1.57 (P-8, 3H; –CH$_3$), 1.62 (P-11, 6H; –CH$_3$), 1.75 (P-21, 6H; –CH$_3$), 1.96 (P-9, 2H; –CH$_2$–), 2.34 (P-10, 2H; –CH$_2$–), 2.88 (P-16, 2H; –CH$_2$–), 3.41 (P-12, 4H; –CH$_2$–),3.43–3.40. (P-19-20, 8H; –CH$_2$–), 3.92–3.93 (P-17-18, 8H; –CH$_2$–), 5.09 (P-14, 4H; =CH$_2$), 5.23 (P-15, 1H; =CH-), 6.25 (P-13, 2H; iso-CH), 6.96 (P-7, 4H; Ar H), 6.98 (P-2, 4H; Ar H), 7.10 (P-4, 8H; Ar H), 7.17 (P-6, 4H; Ar H), 7.18 (P-1, 4H, Ar H), 7.56 (P-5, 4H; Ar H), 7.89 (P-3, 8H; Ar H), respectively.

Preparation of the PAES-*co*-(ZW/PEG)$_2$ membrane

First, the IL–EC mixture was prepared through combining IL and EC in a 7 : 3 (v/v) ratio. LiTf$_2$N was dissolved in the IL–EC mixture to achieve a 0.5 M solution. For PAES-*co*-(ZW/PEG)$_2$ membrane preparation, the dry PAES-*co*-(ZW/PEG)$_2$ solid (0.2 g) was mixed with 70 wt% solution of IL–EC containing LiTf$_2$N, dissolved in 5 mL of THF for 12 h. By employing a doctor blade (model EQ-Se-KTQ150, MTI Co., USA), the solution was uniformly deposited onto a Teflon substrate. PAES-*co*-(ZW/PEG)$_2$ membranes (thickness: 90 ± 5 μm) were obtained after drying at 35 °C for 3 h, followed by vacuum drying at 45 °C for 15 h. The dried membrane was stored in a glove box under argon. For ease of use, the PAES-*co*-(ZW/PEG)$_2$ membrane at different ZW/PEG grafting ratios was abbreviated as PAES-*co*-(ZW*xx*/PEG*yy*)$_2$.

Preparation of the cathode

$LiNi_{0.}5Mn_{1.5}O_4$ (LNMO) and sulfur (S) were used as active cathodic powders for high voltage Li-ion and Li–S batteries. Using a Mini-Mill Pulverisette 23 (Fritsch, Germany), the active materials (80 wt%) were first mixed with conductive graphite (10 wt%). PAES-*co*-(ZW/PEG)$_2$ (10 wt%) as a Li-ion conductive binder was solubilized in NMP solvent (1.0 mL) for 12 h to obtain homogeneous solution. The active material/graphite mixture was combined with the solution dropwise and magnetically stirred for 12 h to form a slurry. Ultrasonication of the slurry was performed for 1.5 h under ambient conditions to achieve homogeneous component distribution. The slurry was spread on 25 μm-thick aluminum foil with a doctor blade (model EQ-Se-KTQ150, MTI Co., USA), followed by vacuum drying at 110 °C for 12 h.

Cell assembly

The PAES-*co*-(ZW/PEG)$_2$ membrane (1.5 cm diameter, $t = 95 \pm 5$ μm) was fabricated in a CR2023 coin-type configuration with a Li foil-based anode (diameter: 1.2 cm; thickness: 0.5 cm) and the prepared cathode (1.2 cm diameter and 95 μm thickness). The loading of the cathodic active material was ∼5.0 mg. All prepared cells were sealed using crimping apparatus (model MSK-160E, MTI Co., USA) and kept inside a glovebox until further analysis.

Characterization and measurement

Chemical structure analysis. The identification of the chemical polymeric structure was conducted by ^{1}H-NMR and FTIR spectroscopic characterization. The NMR spectra were recorded using a Unity Inova instrument (Varian, USA). All samples were dissolved in DMSO-d_6 solvent at 0.1 M for measurement. The FTIR spectra were acquired on a Nicolet iZ10 instrument (Thermo Fisher Scientific, USA) employing an ATR attachment. The wide range of wavenumber length is applied from 3500 to 600 cm^{-1} along with a resolution of 4 cm^{-1}.

Phase separation behavior investigation. The conducting domain spacing (d) was calculated from scattering vector (q) recorded using the small angle X-ray scattering pattern (SAXS). A SAXSess-MC2 apparatus (Anton-Paar company, Austria) in conjunction with a Cyclone Plus phosphor imaging detector (PerkinElmer company, Austria) was employed to collect SAXS curves.

$$d\ (\text{nm}) = \frac{2\pi}{q} \tag{1}$$

Mechanical stability investigation. Mechanical performance metrics (elongation at failure, Young's modulus, and tensile strength) of electrolyte membranes were determined based on stress–strain behavior, which was recorded using a universal tensile tester (Lloyd Instruments, LR30K Plus model, England). The membrane size was prepared at 1 cm × 8 cm × 90 μm for this test.

Thermal properties. The thermal stability of electrolyte membranes (thermal degradation and transition characteristics) was characterized by differential scanning calorimetry (DSC) together with thermogravimetric (TGA) analysis. The TGA curves were obtained using a TG/DTA7300 instrument (Seiko, Japan) in the temperature range of 25–700 °C in a nitrogen environment with a temperature ramp of 10 °C per minute. The DSC data were collected using a DSC-Q20 analyzer (Seiko, Japan) interfaced with an RCS 90 cooling unit (TA Instruments, USA) within −50 to 300 °C at a ramp rate of 5 °C per minute during both thermal ramp-up and ramp-down.

Polysulfide (PS) permeability measurements. All electrolyte membranes with a 5.0 cm diameter and 90 μm thickness were positioned within the glass halves of an H-type cell. To one counterpart a solution composed of DOX, DME, and MeCN in a 1 : 1 : 8 volumetric proportion ($V = 250$ mL) with PS (Co = 0.4 M) was added. The other contained 250 mL of the DOX/DME/MeCN mixture without PS. The PS permeability (P_{PS}) was determined as described below:

$$P_{\text{PS}}\left(\text{cm}^2\text{s}^{-1}\right) = \frac{V \times \tau}{A \times (C_0 - C_\tau)} \times \frac{\text{d}C}{\text{d}\tau} \tag{2}$$

Here, C_τ is the diffusing concentration of PS at various times (τ); dC/dτ corresponds to the slope obtained from the linear regression of C_τ *vs.* τ; and A refers to the working area of the electrolyte membrane (7.07 cm^2). Ultraviolet-visible analysis was carried out with a Varioskan-LUX spectrophotometer (Thermo Fisher Scientific Inc., USA) to collect C_τ. The reaction between S (0.05 mol) with Li_2S (0.01 mol) in a 1 : 1 (v/v) mixture of DOX/DME at 70 °C for 30 h yielded lithium polysulfide.

Electrochemical properties. The bulk resistance (R_{b}) of the electrolyte membrane (1.6 cm diameter, $t = 95$ μm) was used to determine its ionic conductivity (σ_{T}) at various temperatures *via* eqn (3):

$$\sigma_{\text{T}}\left(\text{S cm}^{-1}\right) = \frac{t}{A \times (R_{\text{b}})_T} \tag{3}$$

where A is the area of the electrolyte membrane and $(R_{\text{b}})_T$ is the bulk resistance over a temperature range of −40 to 90 °C using 10 °C steps. The bulk resistance was quantified by a potential electrochemical impedance spectroscopy analysis on a VMP-3 instrument (BioLogic Science Instruments, France) connecting with a TEMP HUMID chamber (DICTH-150SL5, Insight DIC company, Korea) for controlling temperature. The measurement was conducted at 5.0 mV oscillating voltage at frequencies spanning 1 to 10^5 Hz. CR2023 coin cells were assembled in a stainless steel (SS)/electrolyte membrane/SS structure in a glove box. From the σ_{T} *vs.* T plot, the thermal activation energy (E_{a}) was derived according to the following expression:

$$\sigma_{\text{T}} = E_0 \times e^{\frac{-E_{\text{a}}}{RT}} \tag{4}$$

In this expression, E_0 refers to the frequency factor in the Arrhenius equation and R is defined as 8.314 J K^{-1} mol^{-1}, which denotes the universal gas constant.

To determine Li-ion mobility (μ_{Li^+}) and diffusion coefficient (D_{Li^+}), the cell was assembled in an aluminum foil/electrolyte membrane/aluminum foil structure with two pieces of aluminum foil as blocking electrodes and the membrane with 95 μm thickness. The μ_{Li^+} and D_{Li^+} values were calculated from the time of flight (τ), which was obtained from a transient ionic current (TIC) curve. For this test, 0.2 V potential was applied and alternated *via* a reversing switch:

$$\mu_{\text{Li}^+} = \frac{t^2}{\tau \times V} \tag{5}$$

$$D_{\text{Li}^+} = \frac{t^2}{\tau} \tag{6}$$

To evaluate the Li-ion transference number (t_{Li^+}), the lithium (Li)/electrolyte membrane/Li structure was assembled in a cell. The t_{Li^+} was calculated using eqn (7) from chronoamperometry (CA) and PEIS analysis conducted on the VMP3 instrument with an applied voltage ($\Delta V = 10$ mV) for 1800 s. From CA curves, the currents at the early-stage (I_{o}) and steady-level (I_{s}) were obtained. The interfacial resistances at the initial (R_{io}) and stabilized (R_{is}) stages of the CA test were also recorded from the PEIS test.

$$t_{\text{Li}^+} = \frac{I_{\text{s}}(\Delta V - I_{\text{o}} R_{\text{io}})}{I_{\text{o}}(\Delta V - I_{\text{s}} R_{\text{is}})} \tag{7}$$

Electrochemical stability potential of electrolyte membranes was also investigated using linear sweep voltammetry analysis at a 5.0 mV s^{-1} scanning rate at potentials spanning 0 to 8.0 V.

The assembled SS/electrolyte membrane/Li cell was used for this test.

Electrochemical stability at the membrane/lithium anode interface (interfacial stability) was characterized by galvanostatic Li plating and stripping measurement in the lithium/membrane/lithium symmetric cell configuration. This test was repeatedly conducted across a range of current densities of 0.25–1.0 mA cm^{-2} for 60 min per cycle. The measurement at 2.0 mA cm^{-2} was also employed for extended lithium plating and stripping over 1000 h. After that, the Li surface morphology in these tested cells was characterized using a JEOL JSM-7600F microscope (UK).

Cathodic reaction kinetics and polarization were investigated by cyclic voltammetry under the cathode/membrane/lithium cell structure. The cyclic voltammetry tests were performed at room temperature with different scan rates using the VMP3 (BioLogic Science Instrument, France).

Cell performance metrics including charge/discharge capacities, coulombic efficiency (CE) and rate capability along with cycling performance were examined using the VMP3 machine (BioLogic Science Instruments, France) under the cathode/membrane/lithium structure. The electrochemical kinetics (Li-ion diffusion and polarization) of the LSB cell were analyzed using cyclic voltammograms (CVs) at potentials ranging from 1.5 to 2.8 V with multiple sweep rates of 0.2, 0.3, 0.4 and 0.5 mV s^{-1}. The cells underwent cycling within a C-rate range of 0.2–5 C (0.2, 0.5, 1, 2, and 5 C) with 5 cycles at each C-rate and a subsequent return to 0.2 C to assess rate capability. Additionally, continuous cycling at a constant 0.2 C was performed for 200 cycles to evaluate cycling stability. All tests were performed at ambient temperature. Li–S cells underwent charge–discharge cycles over 1.5–2.8 V, while high-voltage Li-ion cells were cycled within 2.8–4.9 V of the voltage window.

Conclusion

A flexible and fast single Li-ion conductive quasi-solid electrolyte, based on PAES-*co*-(ZW/PEG)$_2$, was developed to address the critical challenges of low Li-ion conductivity and the lithium polysulfide migration phenomenon in LSBs. By co-grafting zwitterionic (ZW) and polyethylene glycol (PEG) segments onto the PAES backbone, the ZW segments not only create a robust barrier against polysulfides but also facilitate efficient Li-ion transfer through the membrane. Meanwhile, the flexible PEG segments effectively create rapid Li-ion transport pathways within the robust electrolyte membrane. These synergistic effects result in the PAES-*co*-(ZW/PEG)$_2$ membrane exhibiting a remarkable ionic conduction (1.58 mS cm^{-1}) coupled with a substantial Li-transference number (0.752) at room temperature and excellent mechanical stability (Young's modulus of 15 MPa and a tensile strength of 1.8 MPa). Additionally, the membrane also demonstrates an expanded voltage window extending to 5.28 V and remarkable thermal stability at temperatures reaching 200 °C along with strong interfacial compatibility, evidenced by a low overpotential of 518 mV (only an 8% increase in initial voltage polarization) after 1000 hours of plating/stripping at 2.0 mA cm^{-2}, thus contributing to the inhibition of lithium dendrite propagation. These attributes significantly enhanced the cyclability and rate capability of both LSB cells (93% capacity retention over 350 cycles) and high-voltage lithium-ion battery (LIB) cells (96% retention after 200 cycles) when utilizing PAES-*co*-(ZW40/PEG60)$_2$ as solid electrolyte. This work highlights a novel approach towards achieving highly stable electrochemical performance and effective polysulfide regulation, offering significant potential for advancing the practical development of LSBs and high-voltage LIBs.

Author contributions

Anh Le Mong: investigation, experiments, data curation, formal analysis, visualization, writing – original draft. Jong Chan Shin: experiments, formal analysis, visualization, writing – original draft. Minjae Lee: data curation, visualization, writing – original draft. Dukjoon Kim: validation, conceptualization, methodology, writing – review & editing, supervision.

Conflicts of interest

There are no conflicts to declare.

Data availability

All data are available on request from the authors. All data underlying the results are available as part of the article and no additional source data are required.

Supplementary information (SI) is available. See DOI: https://doi.org/10.1039/d5ta08701e.

Acknowledgements

This work was supported by the Technology Development Program (RS-2024-00509580) funded by the Ministry of SMEs and Startups (MSS, Korea) and the Brain Pool Program (RS-2024-00406414) and the National Research Foundation of Korea (RS-2024-00360494) funded by the Ministry of Science and ICT.

References

1 T. Duraisamy and D. Kaliyaperumal, *J. Green Eng.*, 2020, **10**, 24–61.

2 B. Dunn, H. Kamath and J.-M. Tarascon, *Science*, 2011, **334**, 928.

3 A. Fotouhi, D. J. Auger, K. Propp, S. Longo and M. Wild, *Renew. Sustain. Energy Rev.*, 2016, **56**, 1008–1021.

4 R. Deng, M. Wang, H. Yu, S. Luo, J. Li, F. Chu, B. Liu and F. Wu, *Energy Environ. Mater.*, 2022, **5**, 777–799.

5 Y. Chen, T. Wang, H. Tian, D. Su, Q. Zhang and G. Wang, *Adv. Mater.*, 2021, **33**, 2003666.

6 Y. Fei and G. Li, *Adv. Funct. Mater.*, 2024, **34**, 2312550.

7 A. Manthiram, S.-H. Chung and C. Zu, *Adv. Mater.*, 2015, **27**, 1980–2006.

8 Z. Han, S. Li, Y. Wu, C. Yu, S. Cheng and J. Xie, *J. Mater. Chem. A*, 2021, **9**, 24215–24240.

9 Q. Shao, S. Zhu and J. Chen, *Nano Res.*, 2023, **16**, 8097–8138.

10 M. Xiao, W. Li, M. Yu, B. Lin, D. Peng, Z. Li, S. W. Or, S. Sun and Z. Xing, *Matter*, 2025, **8**, 101934.

11 L. Yin, W. Li, Q. Cao, S. W. Or and Z. Xing, *Chem*, 2024, **10**, 2609–2614.

12 Z. Li, M. Xiao, Q. Cao, C. Guo, M. Yu, D. Peng, Q. Hua, Y. Chen, Y.-Q. Lan and Z. Xing, *Small*, 2025, **21**, e05568.

13 W. Yao, J. Xu, L. Ma, X. Lu, D. Luo, J. Qian, L. Zhan, I. Manke, C. Yang, P. Adelhelm and R. Chen, *Adv. Mater.*, 2023, **35**, 2212116.

14 Q. Wang, J. He, B. Sun, Y. Bai, Y. Yan, J. Xue, Z. Sun, X. Wang, J. Wu, J. Wang, R. Zhao, Z. Sun, H. K. Liu and S. X. Dou, *ACS Nano*, 2025, **19**, 28992–29027.

15 T. Liu, X. Dong, J. Zhang, H. Chen, R. Cao, Z. Sun, W. Zhou, H. Li, D. Chao, Z. Zhou and R. Zhao, *Chem. Sci.*, 2025, **16**, 17426–17435.

16 J. Ma, S. Xing, Y. Wang, J. Yang and F. Yu, *Nano-Micro Lett.*, 2024, **16**, 143.

17 B. Sun, F. Huo, C. Zhao, J. He, J. Xue, Z. Sun, J. Wu, X. Wang, J. Wang, R. Zhao and Z. Sun, *J. Mater. Chem. A*, 2025, **13**, 25444–25456.

18 S. Ohno and W. G. Zeier, *Acc. Mater. Res.*, 2021, **2**, 869–880.

19 Y. Guo, Q. Niu, F. Pei, Q. Wang, Y. Zhang, L. Du, Y. Zhang, Y. Zhang, Y. Zhang, L. Fan, Q. Zhang, L. Yuan and Y. Huang, *Energy Environ. Sci.*, 2024, **17**, 1330–1367.

20 F. Zhao, J. Xue, W. Shao, H. Yu, W. Huang and J. Xiao, *J. Energy Chem.*, 2023, **80**, 625–657.

21 Z.-C. Lv, P.-F. Wang, J.-C. Wang, S.-H. Tian and T.-F. Yi, *J. Ind. Eng. Chem.*, 2023, **124**, 68–88.

22 X. Zhu, L. Wang, Z. Bai, J. Lu and T. Wu, *Nano-Micro Lett.*, 2023, **15**, 75.

23 C. Xian, Q. Wang, Y. Xia, F. Cao, S. Shen, Y. Zhang, M. Chen, Y. Zhong, J. Zhang, X. He, X. Xia, W. Zhang and J. Tu, *Small*, 2023, **19**, 2208164.

24 Z. Cheng, T. Liu, B. Zhao, F. Shen, H. Jin and X. Han, *Energy Storage Mater.*, 2021, **34**, 388–416.

25 Q. Zhang, Q. Huang, S. Hao, S. Deng, Q. He, Z. Lin and Y. Yang, *Adv. Sci.*, 2022, **9**, 2103798.

26 J. Lu and Y. Li, *J. Mater. Sci.: Mater. Electron.*, 2021, **32**, 9736–9754.

27 X. Shan, Y. Zhong, L. Zhang, Y. Zhang, X. Xia, X. Wang and J. Tu, *J. Phys. Chem. C*, 2021, **125**, 19060–19080.

28 X. Chen, C. Zhao, K. Yang, S. Sun, J. Bi, N. Zhu, Q. Cai, J. Wang and W. Yan, *Energy Environ. Mater.*, 2023, **6**, e12483.

29 M. Marcinek, J. Syzdek, M. Marczewski, M. Piszcz, L. Niedzicki, M. Kalita, A. Plewa-Marczewska, A. Bitner, P. Wieczorek, T. Trzeciak, M. Kasprzyk, P. Łężak, Z. Zukowska, A. Zalewska and W. Wieczorek, *Solid State Ionics*, 2015, **276**, 107–126.

30 Z. Li, J. Fu, X. Zhou, S. Gui, L. Wei, H. Yang, H. Li and X. Guo, *Adv. Sci.*, 2023, **10**, 2201718.

31 G. Xi, M. Xiao, S. Wang, D. Han, Y. Li and Y. Meng, *Adv. Funct. Mater.*, 2021, **31**, 2007598.

32 M. K. Tufail, P. Zhai, M. Jia, N. Zhao and X. Guo, *Energy Mater. Adv.*, 2023, **4**, 0015.

33 W.-S. Young, W.-F. Kuan, I. Epps and H. Thomas, *J. Polym. Sci. Part B Polym. Phys.*, 2014, **52**, 1–16.

34 A. Ghosh, C. Wang and P. Kofinas, *J. Electrochem. Soc.*, 2010, **157**, A846.

35 T. C. T. To, A. Le Mong and D. Kim, *J. Mater. Chem. A*, 2025, **13**, 41075–41089.

36 T. C. T. To, A. Le Mong and D. Kim, *J. Mater. Chem. A*, 2025, **13**, 14280–14292.

37 L. Mong Anh and D. Kim, *ACS Appl. Energy Mater.*, 2019, **2**, 2585–2595.

38 A. Le Mong and D. Kim, *Chem.–Eng. J.*, 2023, **456**, 140991.

39 A. Bergfelt, G. Hernández, R. Mogensen, M. J. Lacey, J. Mindemark, D. Brandell and T. M. Bowden, *ACS Appl. Polym. Mater.*, 2020, **2**, 939–948.

40 J. Feng, L. Wang, Y. Chen, P. Wang, H. Zhang and X. He, *Nano Convergence*, 2021, **8**, 2.

41 H. Zhang, H. Han, X. Cheng, L. Zheng, P. Cheng, W. Feng, J. Nie, M. Armand, X. Huang and Z. Zhou, *J. Power Sources*, 2015, **296**, 142–149.

42 J. Atik, D. Diddens, J. H. Thienenkamp, G. Brunklaus, M. Winter and E. Paillard, *Angew. Chem., Int. Ed.*, 2021, **60**, 11919–11927.

43 B. Jiang, V. Ponnuchamy, Y. Shen, X. Yang, K. Yuan, V. Vetere, S. Mossa, I. Skarmoutsos, Y. Zhang and J. Zheng, *J. Phys. Chem. Lett.*, 2016, **7**, 3554–3559.

44 N. Goujon, T. Huynh, K. J. Barlow, R. Kerr, K. Vezzù, V. Di Noto, L. A. O'Dell, J. Chiefari, P. C. Howlett and M. Forsyth, *Batteries Supercaps*, 2019, **2**, 132–138.

45 A. L. Mong and D. Kim, *Energy Storage Mater.*, 2022, **47**, 394–407.

46 D. Penley, S. P. Vicchio, R. B. Getman and B. Gurkan, *Front. Energy Res.*, 2021, **9**, 725010.

47 J. Ha, A. Le Mong, H. Lee and D. Kim, *J. Mater. Chem. A*, 2025, **13**, 42152–42165.

48 X. Tian, Y. Yi, Z. Wu, G. Cheng, S. Zheng, B. Fang, T. Wang, D. G. Shchukin, F. Hai, J. Guo and M. Li, *Chem. Eng. Sci.*, 2023, **266**, 118271.

49 L. Dong, X. Zeng, J. Fu, L. Chen, J. Zhou, S. Dai and L. Shi, *Chem.–Eng. J.*, 2021, **423**, 130209.

50 S. Bandyopadhyay, A. Gupta, R. Srivastava and B. Nandan, *Chem.–Eng. J.*, 2022, **440**, 135926.

51 C. Liu, J. Wang, W. Kou, Z. Yang, P. Zhai, Y. Liu, W. Wu and J. Wang, *Chem.–Eng. J.*, 2021, **404**, 126517.

52 Y. Jin, X. Zong, X. Zhang, Z. Jia, H. Xie and Y. Xiong, *Energy Storage Mater.*, 2022, **49**, 433–444.

53 Z. Zhang, Y. Huang, H. Gao, C. Li, J. Hang and P. Liu, *J. Energy Chem.*, 2021, **60**, 259–271.

54 L. Porcarelli, P. Sutton, V. Bocharova, R. H. Aguirresarobe, H. Zhu, N. Goujon, J. R. Leiza, A. Sokolov, M. Forsyth and D. Mecerreyes, *ACS Appl. Mater. Interfaces*, 2021, **13**, 54354–54362.

55 X. Yu, Y. Liu, J. B. Goodenough and A. Manthiram, *ACS Appl. Mater. Interfaces*, 2021, **13**, 30703–30711.

56 Q. Yang, M. Liao, P. Ren, D. Li, N. Deng, W. Kang and G. Cai, *Chem.–Eng. J.*, 2024, **495**, 153448.

57 M. Liu, X. Guan, H. Liu, X. Ma, Q. Wu, S. Ge, H. Zhang and J. Xu, *Chem.–Eng. J.*, 2022, **445**, 136436.

58 S. Dattilo, C. Puglisi, E. F. Mirabella, A. Spina, A. A. Scamporrino, D. C. Zampino, I. Blanco, G. Cicala,

G. Ognibene, C. Di Mauro and F. Samperi, *Polymers*, 2020, **12**, 1810.

59 N. S. Vrandečić, M. Erceg, M. Jakić and I. Klarić, *Thermochim. Acta*, 2010, **498**, 71–80.

60 Z. Ma, J. Wang, Y. Yang, Y. Zhang, C. Zhao, Y. Yu and S. Wang, *J. Anal. Appl. Pyrolysis*, 2018, **134**, 12–24.

61 S.-K. Cho, K.-S. Oh, J. C. Shin, J. E. Lee, K. M. Lee, J. Cho, W. B. Lee, S. K. Kwak, M. Lee and S.-Y. Lee, *Adv. Funct. Mater.*, 2022, **32**, 2107753.

62 X. Hu, S. R. P. Silva, P. Zhang, K. Liu, S. Zhang and G. Shao, *Chem.–Eng. J.*, 2023, **467**, 143378.

63 W. Liu, K. Zhang, L. Ma, R. Ning, Z. Chen, J. Li, Y. Yan, T. Shang, Z. Lyu, Z. Li, K. Xie and K. P. Loh, *Energy Storage Mater.*, 2022, **49**, 1–10.

64 H. Lu, N. Xu, X. Ni, J. Zhou, J. Liu, Z. Wang, T. Qian and C. Yan, *J. Energy Chem.*, 2021, **58**, 78–84.

65 K. Sun, C. Wang, Y. Dong, P. Guo, P. Cheng, Y. Fu, D. Liu, D. He, S. Das and Y. Negishi, *ACS Appl. Mater. Interfaces*, 2022, **14**, 4079–4090.

66 N. Zhang, B. Li, S. Li and S. Yang, *Adv. Energy Mater.*, 2018, **8**, 1703124.

67 G. Li, F. Lu, X. Dou, X. Wang, D. Luo, H. Sun, A. Yu and Z. Chen, *J. Am. Chem. Soc.*, 2020, **142**, 3583–3592.

68 D. Xiong, S. Huang, D. Fang, D. Yan, G. Li, Y. Yan, S. Chen, Y. Liu, X. Li, Y. Von Lim, Y. Wang, B. Tian, Y. Shi and H. Y. Yang, *Small*, 2021, **17**, 2007442.

69 Y. Chen, G. Zhou, W. Zong, Y. Ouyang, K. Chen, Y. Lv, Y.-E. Miao and T. Liu, *Compos. Commun.*, 2021, **25**, 100679.